Review
doi.org/10.1002/elsa.202200006

Chemistry Europe
European Chemical Societies Publishing

Received: 23 May 2022
Accepted: 24 May 2022

From ion-sensitive field-effect transistor to 2D materials field-effect-transistor biosensors

Silvia Rizzato[1,2] | **Anna Grazia Monteduro**[1,2] | **Angelo Leo**[1,2] | **Maria Teresa Todaro**[2] | **Giuseppe Maruccio**[1,2]

[1]Omnics Research Group, Department of Mathematics and Physics "Ennio De Giorgi", University of Salento and INFN Sezione di Lecce, Lecce, Italy

[2]Institute of Nanotechnology CNR-Nanotec, Lecce, Italy

Correspondence
Giuseppe Maruccio, Omnics Research Group, Department of Mathematics and Physics "Ennio De Giorgi", University of Salento, INFN Sezione di Lecce, Via per Monteroni, 73100 Lecce, Italy.
Email: giuseppe.maruccio@unisalento.it

Silvia Rizzato and Anna Grazia Monteduro equally contributed to the work.

Abstract

Field-effect transistors have strong applications in biosensing field from pH and glucose monitoring to genomics, proteomics, cell signaling assays, and biomedical diagnostics in general. Notable advantages are the high sensitivity (thanks to intrinsic amplification), quick response (useful for real-time monitoring), suitability for miniaturization, and compact portable read-out systems. The initial concept of ion-sensitive field-effect transistors evolved with the emergence of novel classes of materials beyond traditional semiconductors. Recently, 2D nanomaterials are redesigning the field providing superior performances with large surface-to-volume ratio, high carrier mobility, more effective local gating, high transconductance, and operation at low voltages. Here, after a brief conceptual introduction, we review progresses and perspectives of 2D materials field-effect-transistor biosensors with special focus on opportunities, most recent applications, present challenges, and future perspectives.

KEYWORDS
biosensing, field-effect-transistor, graphene, ISFET, transition metal dichalcogenides, two-dimensional nanomaterials

1 | INTRODUCTION

The application of field-effect transistors (FETs) for the implementation of biosensors can be traced back to the seventies when ion-sensitive solid state devices were proposed by Bergveld.[1] pH sensing was among the first applications.[2] In 1980, Janata group reported FET-biosensors for detecting penicillin using an enzyme-modified gate.[3] Successively, the basic concept of ion-sensitive field-effect transistor (ISFET) and chemical/biological FET was tuned in various forms depending on the target application (gene/DNA-modified FET [GenFET], immunologically modified FET [ImmunoFET], and enzyme-modified FET [EnFET])[4] or the employed materials.[2,5]

Notable advantages are the high sensitivity (thanks to intrinsic amplification), quick response (useful for real-time monitoring), suitability for miniaturization, and compact portable read-out systems.[2,6] Furthermore, no preprocessing of the target analyte is typically necessary. Today, the principal application of ISFET concerns the evaluation of ion concentration changes in solutions

Review
doi.org/10.1002/elsa.202200006

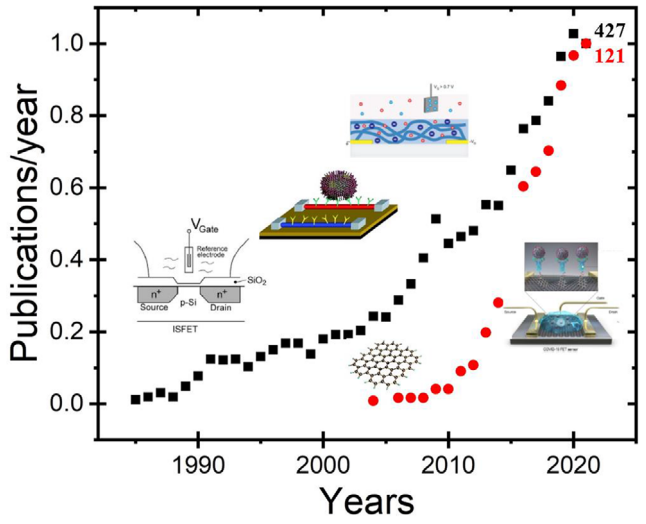

FIGURE 1 Trends in FET biosensors (black curve) and recent emergence of 2D materials FET biosensors (red curve) in terms of publications per year. For facilitating a direct comparison of the growing trends, both curves are normalized to unit in their maximum value by dividing for factors 427 and 121, respectively, which correspond to total numbers of publications per year in both fields in the last available year (2021). The inset on G-FET is adapted from Ref.[10] with permission; Copyright American Chemical Society, 2020

related to the difference of potential between the Fermi level of the semiconductor and the solution redox potential.

With the advent of nanomaterials, and nanowires in particular, a strong progress was achieved, exploiting their inherent large surface-to-volume ratios, which favor high sensitivity.[7] Low-cost organic transistors also gained considerable interest for biosensing purposes, either in the form of electrolyte gated organic field-effect transistor and organic electrochemical transistor.[8] More recently, graphene and 2D materials are having a strong impact by exploiting their high charge-carrier mobility and chemical robustness.[9]

Here, after a brief conceptual discussion on FET-biosensors, we review progresses and perspectives of 2D materials field-effect-transistor biosensors with special focus on opportunities and most recent applications, favored by large surface-to-volume ratio, high carrier mobility, more effective local gating, high transconductance, and operation at low voltages. The large interest in the field is demonstrated by the increasing number of publications as shown in Figure 1. In particular, for a more direct comparison of the growing trends, the values for FET biosensors and 2D materials FET biosensors were divided by the total numbers of publications in both fields, which in the last available year (2021) were 427 and 121, respectively, as indicated in the top right corner.

2 | FET BIOSENSOR WORKING PRINCIPLE

The idea at the basis of FET biosensors is as simple as it is ingenious.[2] In a normal metal-oxide semiconductor field-effect transistor (MOSFET), the current flowing in the channel among source and drain electrodes can be gate-modulated by means of a field effect, which determines accumulation or depletion of mobile charge carriers, which are attracted or repelled depending on their type and the direction of the field. As a result, the drain-source current (I_{ds}) for a fixed drain-source voltage increases or decreases, since it is strictly connected to the amount of available charge carriers in the channel (Figure 2a).

This mechanism can be exploited for biosensing purposes with just a few changes. The architecture is basically constituted again by a semiconductor support on which the source and drain electrodes are fabricated. However, the transistor is placed in a solution with the necessary layer passivation to avoid disturbances during measurements, and the gate electrode is replaced with a reference electrode (Figure 2b). The biorecognition surfaces are either an extension of the gate contact or the gate oxide itself. Any charge density at the solid–liquid interface in proximity of the gate dielectric layer has the same effect of an applied gate voltage in a MOSFET, since it results in an electric field which modulates the mobile charge carrier density (Figure 2c). In the most common case, a pH sensing layer is placed in contact with a solution-gate, which controls the current flow in the device channel.[11] The output drain-source current can be then strictly correlated to the concentration of analytes (e.g., H^+ ions) determining the local charge variation, that is, the pH value (Figure 2b,c), the amount of adsorbed DNA targets (Figure 2d) or antigens (Figure 2e), the result of an enzyme-catalyzed reaction (Figure 2f), or the opening of transmembrane channels in cells resulting in ions release and nerve cell signaling (Figure 2g). Thus, DNA strands hybridization, antigen–antibody interactions, or enzyme–substrate reactions can be employed to provide specificity to FET biosensors as in the case of other transducers (e.g., in the case of optical, electrochemical, impedance, or acoustic transduction[12]).

Beyond local electric fields and changes in the density or mobility of charge carriers in the conducting channel, other mechanisms responsible for changes in the response of BioFET can be variations of capacitance in the bulk semiconductor and in the biofunctionalized layer realized for biorecognition.[13] In this respect, the dielectric layer/materials play an important role in determining the overall device response, and this aspect triggered FET research on novel dielectric (e.g., high k) materials for

Review
doi.org/10.1002/elsa.202200006
Chemistry Europe
European Chemical Societies Publishing

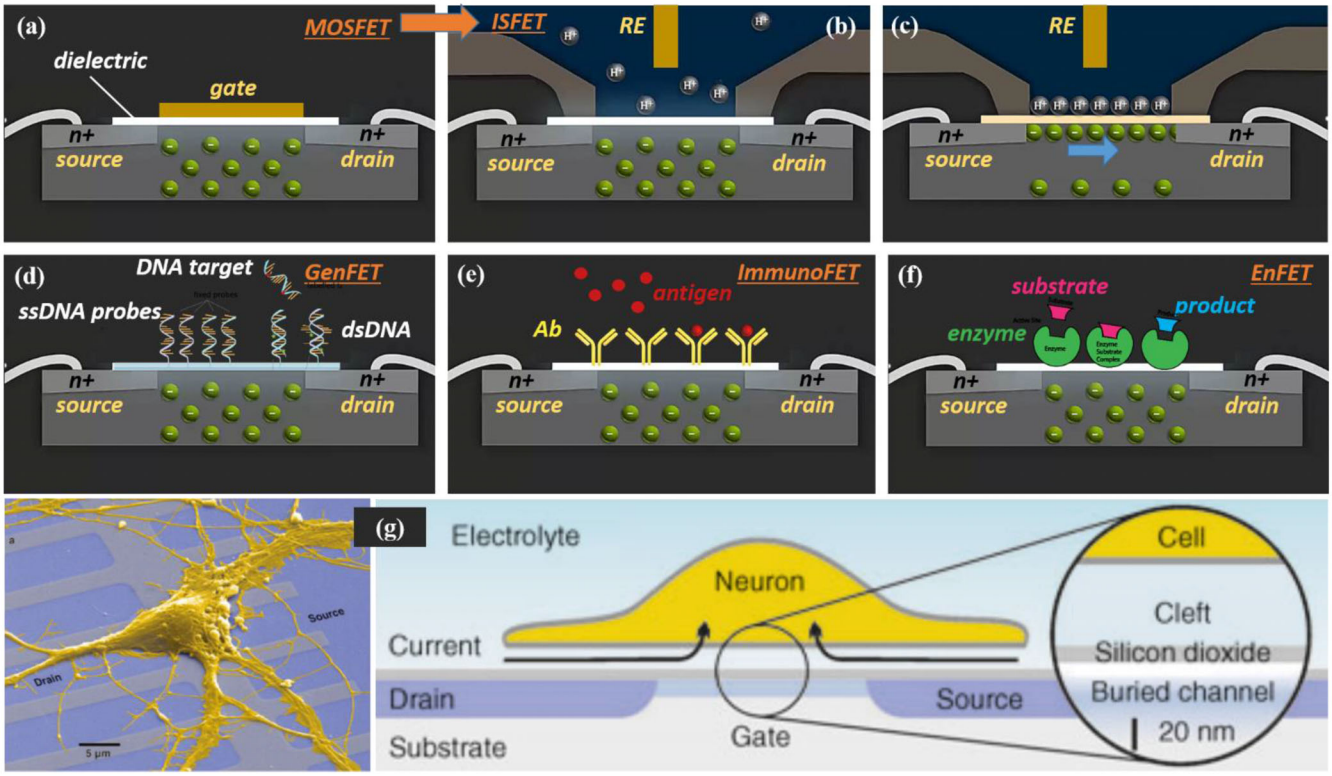

FIGURE 2 Schemes and working principle of (a) a MOSFET based on a generic semiconductor, where the carrier density in the channel is modulated by the gate voltage applied through a gate electrode (dark yellow) on top of a gate insulator (thin white layer); (b) an ISFET, where the gate electrode is replaced by a reference electrode (RE) in the solution and the channel carrier density depends on the amount of charges (ions) close to the interface, for example (c) the presence of H^+ ions attracts electrons in the channel increasing the measured current at fixed drain-source voltage and making ISFET sensitive to ion concentration (pH or other ions too with the integration of ion-selective surfaces); (d–f) GenFET, ImmunoFET, and EnFET variants, where the sensor response depends on the amount of local (charged) analytes near the interface (e.g., DNA is negatively charged) and the associated electric fields upon DNA hybridization (from single-stranded DNA [ssDNA] to double-stranded DNA [dsDNA]), antigen-antibody (Ab) recognition, and enzyme–substrate reaction. (g) bioFET application for readout of nerve cell signals, where the ion released by the cells through their activated ion channels is responsible of the modulation of the channel carrier density (this last part of the figure is reproduced from Ref.[15] with permission)

electronic applications and ion-selective films and dielectric modulation for biosensing.[14]

The previous discussion was based on a standard semiconductor MOSFET. However, the concept can be straightforwardly extended to other transistor architectures, including high electron mobility transistors, organic transistors, nanowire FETs, or 2D material FETs. It is worth noting as this transduction approach is very compatible with electrochemical experimental setups with the advantages of intrinsic signal amplification and miniaturization opportunities.

3 | 2D MATERIALS—PROPERTIES AND OPPORTUNITIES

Before discussing 2D materials field-effect-transistor biosensors, it is useful to recapitulate some peculiarities of graphene and its 2D analogues and consequently devices. Graphene was highly investigated long before it became experimentally accessible.[16] The reason is the unique set of long speculated properties it was expected to exhibit.[17]

Graphene honeycomb lattice can be regarded as a triangular lattice with a two atoms basis per unit cell or two interlocking triangular sublattices (A and B in Figure 3a). The Brillouin zone reflects this symmetry and presents two inequivalent (Dirac) points K and K' (Figure 3a, right). A tight-binding Hamiltonian allows to catch the peculiar physics of carriers in graphene. As illustrated in Figure 3b-top, it results in valence and conduction bands touching in correspondence of the K and K' points in whose proximity the electronic dispersion can be expanded resulting to be linear (at first order) and gives the famous Dirac cones, which describe carriers as massless Dirac fermions with an effective speed of light v_F and a 2D pseudospin (associated with valleys). This is strikingly different from the standard case of a traditional semiconductor, where the carriers are described as standard Schrödinger

Review
doi.org/10.1002/elsa.202200006

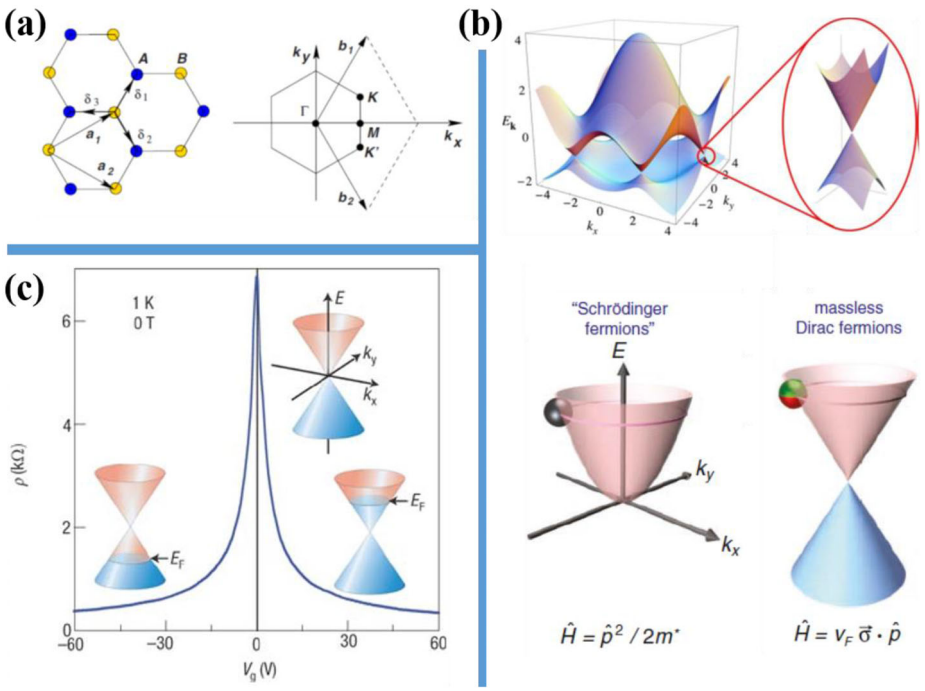

FIGURE 3 (a-left) Honeycomb graphene lattice showing in different colors (blue and yellow) the atoms in the two interlocking constituent sublattices (A and B), δ_1, δ_2, δ_3 and a_1, a_2 are the unit vectors connecting the atoms with, respectively, the nearest neighbors and next-nearest neighbors; (a-right) corresponding first Brillouin zone with indication of more relevant points and directions, including the two inequivalent (K and K') Dirac points at the vertex and the unit vectors b_1 and b_2 of the reciprocal lattice (reproduced from Ref.[17] with permission; Copyright American Physical Society, 2009); (b) graphene bands showing energy dispersion as a function of the wavevector components k_x and k_y with detail on the Dirac cones and comparison among Schrodinger and massless Dirac fermions with corresponding dispersion plots and describing equations, where m* is the electron effective mass, p is the momentum, v_F is the Fermi velocity, σ = 2D pseudospin matrix describing the two sublattices (reproduced from Refs. [17, 18] with permission); (c) ambipolar behavior in charge transport showing the typical response with a resistivity (ρ) maximum (corresponding to a minimum in conductivity [σ] or drain-source current [I_{ds}]) when the gate voltage V_g crosses the Dirac point associated with the change from hole to electron carrier transport as also sketched in the insets showing the shift of the Fermi energy within the Dirac cones (reproduced from Ref.[19] with permission; Copyright Nature Publishing Group, 2007)

fermions with effective mass m* associated with a traditional paraboloid dispersion (Figure 3b-bottom). In other words, as noticed by the Nobel award winner Geim, the resulting physics is more similar to that tested at CERN than to normal condensed matter physics, and relativistic effects can be observed. Noteworthy, this scenario characterizes graphene monolayer (and some analogues) but strongly changes with two or more layers.

Among the consequence of such peculiar energy dispersion relevant for biosensing purposes, graphene behaves as a semimetal, that is, a zero gap semiconductor, with electron-hole symmetry and exhibits an ambipolar nature with the ability to continuously tune the charge carriers from holes to electrons (Figure 3c). The transfer characteristic of a graphene FET reproduces a similar trend and differs from that of a MOSFET. In this case, biosensors can be fabricated monitoring changes in Dirac point shift or consequent resistance variations.

Despite the large success of silicon and germanium in modern electronics, atomically thin materials are on the rise since they have shown peculiar properties, such as high electron mobilities,[20] tunable properties, near room temperature topological insulation,[21] and alkali-ion storage capability.[11,20] After graphene breakthrough discovery, 2D materials attracted research attention for potential applications in electronic and optoelectronic devices, and today, graphene analogues include elemental 2D materials, 2D chalcogenides, MXenes, and 2D oxides. These 2D materials exhibit a large range of behaviors from insulator to semiconductor, half-metal, semi-metal, metal, and superconductor as summarized in Figure 4. As a result, their applications in several fields can be envisaged.

4 | GRAPHENE-BASED FET BIOSENSORS

Graphene-based FET biosensors have the 2D material deposited on an insulating (typically SiO_2) layer and interconnected through source and drain electrodes. Both

Review
doi.org/10.1002/elsa.202200006
Chemistry Europe
European Chemical Societies Publishing

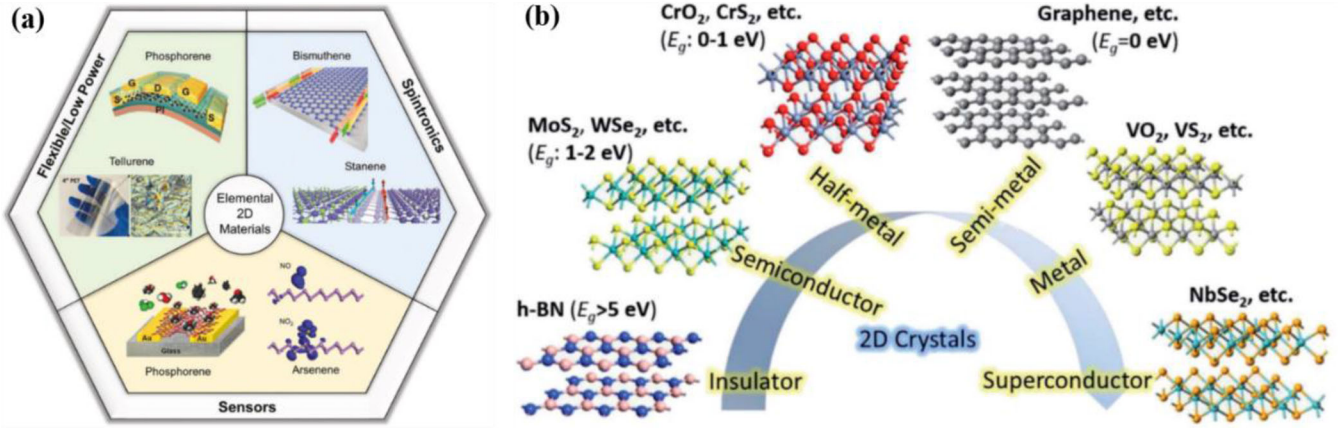

FIGURE 4 (a) Elemental 2D materials and their potential applications from sensors (phosphorene, arsenene), to flexible and low-power applications (phosphorene, tellurene) and spintronics (bismuthine, stanine). (b) Other two-dimensional materials beyond graphene with a large variety of electrical behaviors, from insulator (h-BN), semiconductor (MoS_2, WSe_2), half-metal (CrO_2, CrS_2), semi-metal (graphene), metal (VO_2, VS_2), and superconductor ($NbSe_2$) and potential applications (reproduced with permission from Ref.[22] and reproduced from Ref.[23])

back-gated or liquid-gated architectures have been investigated. Remarkably, strengths of biosensors based on graphene or graphene oxide field-effect transistors (G-FET and rGO-FET) are their large surface-to-volume ratio and high carrier mobility. Furthermore, their channel consists of atomic monolayers and, for this reason, the charged species (analytes) are in its strong proximity or directly attached to the channel and modulate more efficiently the electric field and the device response. In graphene-based architectures, the gate dielectrics is replaced by the electrical double layer (EDL) at the solid–liquid interface, where the V_{GS} drops and the EDL high capacitance permits a more effective local gating and operation at low voltages and high transconductance, which are both advantageous figures for biosensing applications since they improve sensitivity and limit of detection (LOD).[24] The readout scheme is based on the induced change in the Dirac voltage, a feature characteristic of the ambipolar nature of conduction in graphene and corresponding to the gate voltage required for minimizing the device conductance (Figure 3c). This is reflected by a measurable change in the drain-source current, which can be correlated to the analyte concentration. A further advantage is that no labeling is necessary for detection.

Despite graphene-based FET biosensors are still in their infancies, in a few years, several proofs of concept were reported. For genomic applications, G-FET and rGO-FET attained remarkable performance when compared to the technological alternatives consisting of polymerase chain reaction, optical, and electrochemical techniques, in particular, if target amplification steps want to be avoided. Notably, a DNA LOD in the sub-fM range was achieved, which is orders of magnitude better than for other direct transducers (commonly in the pM range). The first reports on DNA detection with G-FET started in 2011 and were characterized by decreasing LOD (from 1 nM to 1 pM) as the devices underwent optimization.[25] More recently, Xu et al. functionalized the graphene layer with biotinylated BSA, streptavidin, and then biotinylated DNA probes and demonstrated a further reduction of the LOD to 100 fM matching the performance of optical DNA microarrays.[26] The use of chemical vapor deposition (CVD) to grow graphene provides samples with large 2D morphology and allows to reduce contamination possibilities with respect to most common methods based on transferring graphene on the device substrate.[27]

In 2015, Zheng et al. reported another G-FET biosensor based on CVD-grown graphene, but in this case, the molecular probes consisted of peptidic nucleic acids (PNAs), which were immobilized on the G-FET channel using 1-pyrenebutanoic acid succinimidyl ester (PASE) as crosslinker. PNAs present the advantage of minimizing the electrostatic repulsion in the hybridization process since the PNA backbone is neutral as opposite to the negatively charged DNA backbone. This approach allowed to reach an LOD as low as 10 fM. Furthermore, the authors reported a prominent selectivity with a negligible response when exposed to noncomplementary and one-base-mismatched DNA. PNA–DNA hybridization was investigated by Cai et al. using rGO-FET biosensors too.[28]

The length of the DNA probes and target chains affects the target-probe affinity and ultimately the LOD, which was reported to be 100 pM for 22 mer and 1 fM for 60 mer target DNA.[29] This aspect can pose severe limitations when short sequences are targeted as it is sought for early diagnosis of cancer, cardiovascular, and other

diseases. Notably, this constraint was overcome by Gao et al., which demonstrated sub-fM range LOD for a 21 mer target DNA using engineered hairpin probes (especially designed ssDNA with excellent sensing specificity) and triggered self-assembly amplification.[30] Specificity of these biosensors was high, permitting to distinguish single-base mismatched oligomers.[30] Campos et al. even reached attomolar LOD with electrolyte-gated G-FETs.[24] Still within genomic applications, a relevant task is to have tools able to detect single nucleotide polymorphisms (SNPs, i.e., single nucleotide substitution at a specific position) with high sensitivity and specificity since this is relevant for genetic epidemiology and to determine genetic variants associated with diseases. In this respect, it is worth noting as Hwang and coworkers reported graphene field-effect transistors (G-FET) able to quantitatively detect SNP with picomolar sensitivity, which corresponds to an improvement of more than 1000-fold in sensitivity.[31] Furthermore, their platform was implemented with a wireless data transmission system.

Apart from DNA, G-FET and rGO-FET were used to implement immunosensors and detect biotin,[32] interleukin-6,[33] insulin,[34] prostate-specific antigen,[35] small antigen peptides, such as antigen osteocalcin peptide BGP-C7,[36] hormones, such as the antidiuretic hormone,[37] chemical compounds, such as bisphenol A,[38] interferon gamma,[39] small-molecule drugs,[40] human immunodeficiency virus, and associated cardiovascular and arthritis diseases.[41] Tables 1 and 2 summarize the literature results for G-FET and rGO-FET biosensors in terms of target molecule/probe, detection limit, and sensitivity and/or related measurements. Notably, LODs in the fM and sub-fM range can be noticed for DNA, protein (e.g., insulin), or drug detection. In many cases, specificity has been also tested, as this parameter is crucial for quantifying the ability to distinguish the target analyte with respect to other analyte coexisting in the same solution. Response times from few minutes (260 s)[34] down to 1 s[42] were reported. In general, thanks to a higher transconductance, G-FET biosensors using single-layer graphene exhibit higher performance with better LOD than in the case of few layer graphene or rGO-FET.[24]

A paradigmatic case of graphene-based FET biosensors in terms of responses and sensitivity is reported in Figure 5, which allows to explain in more detail (with the support of images and schemes) the readout mechanism and the different effect the analytes can have depending on the sign of their electric charge. Specifically, Park and coworkers focused on two Alzheimer's disease biomarkers Aβ_{1-42} and t-Tau providing a tool for their multiplexed detection (Figure 5a,b).[58] The functionalization strategy was based on the use of 1-pyrenebutyric acid N-hydroxysuccinimide ester (PBASE) as cross-linker, which binds on one side to the rGO surface through pyrene group and π–π staking interactions, on the other side to the antibodies via an amine group. This procedure can be considered as a general approach for the immobilization of molecular probes on G-FET and rGO-FET biosensor channels to provide them the desired selectivity. Upon incubation with the target analytes, since Aβ_{1-42} and t-Tau are, respectively, negatively and positively charged in physiological conditions, their recognition through immobilized specific antibodies influences the G-FET biosensor response by n-doping and p-doping effect leading to Dirac point shifts in opposite directions (Figure 5a), namely, left-shifted for Aβ_{1-42} and right-shifted for t-Tau. This is indeed observed in the transfer characteristics plot of the drain-source current I_{ds} versus the gate voltage V_G shown in Figure 5c,d and is reflected in the corresponding calibration curves (Figure 5e,f) reporting a quite linear shift of the Dirac point ΔV_{Dirac} as a function of the biomarker concentrations in the range from 100 fg/ml to 100 ng/ml (with a slope, respectively −15.63 mV*ml/pg and +22.96 mV*ml/pg). Notably, the authors demonstrated strong specificity of the assays when testing the response in presence and in combination with possible interfering analytes, such as the amyloid protein alpha-synuclein (α-syn, associated with dementia and neurodegenerative diseases) and the brain-derived neurotrophic factor (BDNF, a biomarker associated with Alzheimer's disease and depression) (Figure 5g,h). Indeed, small ΔV_{Dirac} shifts (less than 10 mV) were observed in the absence of the analyte corresponding to the immobilized antibody in contrast to much higher values (above 30 mV) in their presence. Good responses were reported when operating with peptide-spiked solutions in PBS, artificial cerebrospinal fluid, and human plasma. In particular, the last two cases are relevant since neurodegenerative disease biomarkers are present in higher concentration in cerebrospinal fluid and more diluted in human plasma, which, however, has the advantage of being more easily accessible for diagnostic purposes.

Similarly to traditional semiconductor-ISFET field, enzyme-modification of reduced graphene oxide field-effect transistors (rGO-FET) was employed for monitoring glucose,[43] urea,[59] arginine with cascading enzymes,[57] and drug effects in Alzheimer's disease treatment.[60] In some cases, graphene was decorated with gold nanoparticles for DNA, lactose, or microRNA detection[44–45,61] or palladium nanoflowers for glucose detection.[46] Other modifications include the combination with carboxylated polypyrrole nanotubes for glucose biosensors,[67] the integration of electrosynthesized amino moiety bearing polymer layers,[54] and the use of a graphene foam for ATP biosensors.[53] Remarkably, a rGO-FET olfactory biosensor was reported by Larisika et al., where functionalization

TABLE 1 Overview of the performances and key parameters of G-FET biosensors

Target molecule/probe	Limit of detection	Sensitivity, response, and/or related measurements	Ref.
DNA target/DNA probe	25 aM	24 mV/decade for Dirac voltage shift (1 aM–10 fM)	[24]
DNA target/PNA probe	10 fM	V_{CNP} shift versus DNA concentration (1 fM–100 pM) [CNP: charge-neutrality point or Dirac point]	[27]
DNA target/DNA probe	~5 fM	Dirac voltage shift versus DNA concentration (1 fM–1 μM)	[30]
DNA target/DNA probe	pM	Dirac voltage shift versus DNA concentration (100 pM–100 nM)	[31]
Biotin/avidin	0.37 pM	Langmuir fitting of ΔI_{ds} versus biotin concentration	[32]
Interleukin-6 (IL-6)––insulin/PASE	618 fM (IL-6) 766 fM (insulin)	Hill–Langmuir fitting of ΔI_{ds} at different target concentration up to 10 μM	[33]
Insulin/IGA3 aptamer	35 pM	Hill–Langmuir fitting of ΔV_{Dirac} versus concentration (0.1 nM–1 μM)	[34]
BGP-C7/anti-bone Gla protein (BGP or osteocalcin) antibody	10 fg/ml	$\Delta I_{ds}/g_m$ versus concentration (10^{-5} to 10^{2} ng/ml) (g_m = transconductance)	[36]
ADH protein/ADH-specific aptamer (ADH = antidiuretic hormone)	3.55 ag/ml	50.00 μA $(g/ml)^{-1}$	[37]
Bisphenol A (BPA)/DNA molecules	10 ng/ml	Dirac point V_g and I_{ds} versus BPA concentration (1–100 μg/ml)	[38]Δ
IFN-γ target/IFN-γ aptamer (IFN-γ: interferon-gamma)	83 pM	Lorentzian fitting of I_{Dirac} versus IFN-γ concentration (2 nM–100 μM)	[39]
Kinase Abl1 protein target/imatinib drug	15.5 fM	~0.0194 μA/fM (20–100 fM)	[40]
p24-cTn1-CCP biomarkers/corresponding antibodies [cTn1: cardiac troponin 1; CCP: cyclic citrullinated peptide]	100 fg/ml for p24 10 fg/ml for cTn1 and CCP	ΔR(%) versus antigens concentration (linear response from 1 fg/ml to 1 μg/ml)	[41]**
Glucose detection/glucose oxidase (GOx) enzyme entrapped in silk film	0.1 mM	2.5 μA/mM (0.1–13 mM)	[43] *
DNA detection/DNA aptamer Streptavidin/DNA aptamer	15 aM (DNA) ≈ 9 aM (streptavidin)	8 mV/decade (ΔV_{CNP}) (1 aM–1 pM) (DNA) 14 mV/decade (1 aM–1 fM) (streptavidin)	[44]
Lactose detection/human galectin 3 (CRD hGal-3 M249C)	200 aM	$\Delta V_{CNP} = -0.00724*\log[C_{lactose}] - 0.26454$	[45]
Glucose/glucose oxidase	1 nM	$\Delta I_{DS}/I_0$ versus glucose concentration linear in (10 nM–10 μM) range	[46]
Exosomes detection/anti-CD63 antibodies	0.1 μg/ml	Not determined	[67]
Hg detection/aptamer (3′-amine-TTC TTT CTT CCC CTT GTT TGT-C10 carboxylic acid-5′)	10 pM	$\Delta I_{DS}/I_0$ versus Hg concentration (10 pM–100 nM)	[42]
17β-estradiol (E2)/different DNA aptamers	34.70 pM	Differential response versus E2 concentration in the presence of pH interferences	[47]
Escherichia coli (*E. coli*) detection/pyrene-tagged DNA aptamers	10^2 CFU ml^{-1}	2.5×10^{-3} μA per CFU ml^{-1}	[48]

(Continues)

Chemistry Europe
European Chemical Societies Publishing

TABLE 1 (Continued)

Target molecule/probe	Limit of detection	Sensitivity, response, and/or related measurements	Ref.
Gram-negative (GNB) and––(GPB) positive bacteria/antibiotic (vancomycin and magainin I)	1–9 CFU/ml	Dirac voltage shift when adding target bacteria (*E. coli* and *S. aureus*) at specific concentration	[49]
Bacteria (*S. aureus* and *A. baumannii*)/pyrene-conjugated peptide probes (P-KAM5 and P-KAM8)	10^4 cells/ml	Resistance versus liquid gate voltage and Dirac voltage shift versus bacteria concentration	[50]
SARS-CoV-2/specific antibody [SARS-CoV-2 severe acute respiratory syndrome coronavirus 2]	1 fg/ml in solution 1.6×10^1 pfu/ml in culture medium 2.42×10^2 copies/ml in clinical samples	$\Delta I/I_0$ versus concentration (1–10^4 fg/ml)	[10]
Blood samples with different activators (vitamin K, calcium chloride, and thromboplastin reagent) and inhibitors (heparin drugs)	–	–	[51]
Lactic acid/lactic acid oxidase	30 nM for H_2O_2 300 nM for lactic acid	ΔV_{Geff} versus log [lactic acid] with a slope of 43 mV/decade (3–300 μM)	[52]
Adenosine triphosphate (ATP)/APT aptamer	0.5 pM	Linear ΔI_{DS} versus log[C_{ATP}] from 0.5 pM to 50 μM	[53]

Note: Typically 2D materials are single layer: for materials with double layers, the Ref. is indicated as []*, while in case of more than two layers (multilayer), the Ref. is indicated as []**. The carrier mobility, where reported, spans from 605 $cm^2 (Vs)^{-1}$ (Ref.[27]) to 2700±700 $cm^2 (Vs)^{-1}$ (Ref.[30]). The I_{on}/I_{off} ratio has not been reported in many cases and, for this reason, is not indicated in the table too. Response time, where reported, shows a range between < 1 s (Ref.[42]) and 260 s (Ref.[34]). Selectivity experiments have been performed in all works, except those whose Ref. is indicated as []$^{\Delta}$. The last line regards a work employing graphene foam. CFU stays for colony-forming unit.

Chemistry Europe European Chemical Societies Publishing

TABLE 2 Overview of the performances and key parameters of rGO-FET biosensors

Target molecule/probe	Limit of detection	Sensitivity, response, and/or related measurements	Ref.
DNA target/PNA probe	100 fM	V_{CNP} shift versus DNA concentration (10 fM–1 nM)	[28]
PSA–ACT complexes/PSA monoclonal antibodies [PSA-ACT: prostate-specific antigen/a1-antichymotrypsin]	100 fg/ml (~1.1 fM)	-20 ± 4.0 mV/decade and $+20 \pm 4.5$ mV/decade for ΔV_{Dirac} versus concentration at two different pH (100 fg/ml–1 mg/ml)	[35]
$A\beta_{1-42}$––t-Tau biomarkers/specific antibodies	fM	$\Delta V_{Dirac} = -15.63 \log[C_{A\beta 1-42}] - 25.26$ $\Delta V_{Dirac} = 22.96 \log [C_{t\text{-}Tau}] + 55.85$	[58]
Urea detection/urease-polyethylenimine (PEI) multilayer	1 μM	20.3 ± 0.6 μA/pH for RGO/SPS/FET 25.9 ± 0.6 μA/pH for RGO/SPS/PEI/FET 9200 ± 500 $\mu A/cm^2$ per decade of [urea] for (PEI/urease)3-RGO FETs [SPS: negative charged pyrene-based layer of sodium 1-]	[59]
L-arginine/arginase-urease-PEI system	10 μM	Slope of 33.5 μA per decade (10–1000 μM)	[57]
Acetylcholine (ACh)/acetylcholinesterase (AChE) Aβ protein/monoclonal 6E10 antibody		24.12 mV pH^{-1} (pH range: 4–10) ΔV_{Dirac} versus $\log[C_{Ach}]$ with 13.9 mV dec^{-1} slope of the linear fit ΔV_{Dirac} versus $\log[C_{A\beta}]$ with 12.51 mV dec^{-1} slope of the linear fit	[60]$^{\Delta}$
miRNA/peptide nucleic acid (PNA) probe	10 fM	ΔV_{CNP} versus miRNA concentration (1 fM–100 pM)	[61]**
Acetylcholinesterease (AchE)/acetylcholine	2.3 μM	-26.6 ± 0.7 μA/Ach decade (5 μM–1 mM)	[54]
Odorant detection (methyl vanillate, methyl eugenol et al.)/protein 14 (OBP14)	–	Langmuir isotherms of eugenol and methyl eugenol and affinity constants for several odorants	[62]$^{\Delta}$
Exosome/antibody CD63	33 particles/μl	$-\Delta V_{CNP} = 11.6*\log[C_{expspme}] - 40$	[63]
HepG2 cell-derived microvesicles/sulfhydrylated HepG2 cell-specific TLS11a aptamer (AptTLS11a) and epithelial cell adhesion molecule aptamer (AptEpCAM)	84 particles/μl	$-\Delta V_{CNP} = -113.1+25.4*\log C$	[64]
E. coli/anti *E. coli*	10^3 CFU ml^{-1}	Linear fitting of $\Delta R/R_0$ versus *E. coli* concentration from 10^3 to 10^6 CFU/ml	[56]
Human papillomavirus (HPV-16 E7)/RNA aptamer Sc5-c3	100 pg ml^{-1}	Langmuir isotherm fitting of $\Delta I/I_0$ versus concentration (1 nM–1 μM)	[55]$^{\Delta}$
Nitric oxide (NO) detection	1 pM in (PBS) 10 pM in the cell medium	$\Delta I(nA) = 79.4* \log C_{NO}(M) + 1000$ in PBS $\Delta I(nA) = 72.7*\log C_{NO}(M) +830.7$ in the cell medium	[65]
Glutamate/metabotropic glutamate receptors (mGluR)	1 fM	$\Delta I/I_0$ (%) $= 0.2305*\log C_{GLU}(M)+3.539$	[66]
Glucose/glucose oxidase	1 nM	$\Delta I_{DS}/I_0$ versus glucose concentration (1 nM–100 μM)	[67]

Note: Typically 2D materials are single layer: for materials with double layers, the Ref. is indicated as []*, while in case of more than two layers (multilayer), the Ref. is indicated as []**. The carrier mobility, where reported, spans from 12 $cm^{[2]}$ $(Vs)^{-1}$ (Ref.[54]) to 725 and 680 $cm^{[2]}$ $(Vs)^{-1}$ (for electrons and holes, respectively) in Ref.[55] The I_{on}/I_{off} ratio has not been reported in many cases and, for this reason, is not indicated in the table too. Response time, where reported, shows a range between 50 s (Ref.[56]) and 180 s (Ref.[57]). Selectivity experiments have been performed in all works, except those whose Ref. is indicated as []$^{\Delta}$. The last line regards a work employing RGO––C-PPy NT hybrids (where C-PPy NT is carboxylated polypyrrole nanotube).

doi.org/10.1002/elsa.202200006

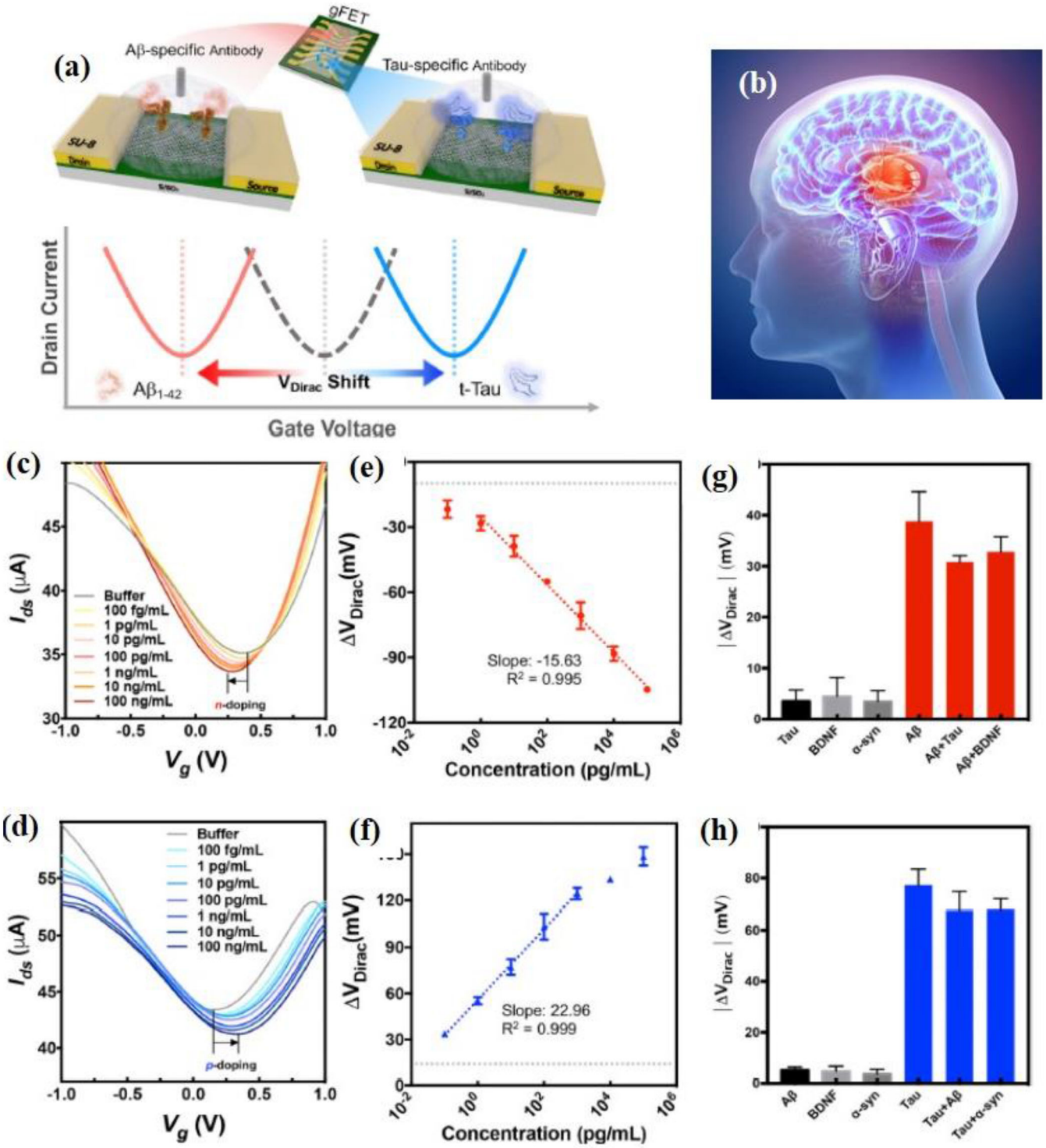

FIGURE 5 (a,b) G-FET biosensors for detection of Alzheimer's disease biomarkers Aβ_{1-42} and t-Tau having opposite charges in physiological conditions and thus resulting in Dirac point shift in opposite directions. (c–f) Transfer characteristics plot of the drain-source current I_{ds} versus the gate voltage V_G and calibration curves of the Dirac point shift ΔV_{Dirac} as a function of the biomarker concentrations in the range from 100 fg/ml to 100 ng/ml for Aβ_{1-42} (c–e) and t-Tau (d–f), respectively. (g,h) The graphs demonstrated strong specificity of the assays for Aβ_{1-42} (g) and t-Tau (h) when testing the response in presence and in combination with possible interfering analytes, such as the amyloid protein alpha-synuclein (α-syn, associated with dementia and neurodegenerative diseases) and the brain-derived neurotrophic factor (BDNF, a biomarker associated with Alzheimer's disease and depression). Reproduced from Ref.[58] with permission; Copyright Elsevier B.V., 2020

doi.org/10.1002/elsa.202200006

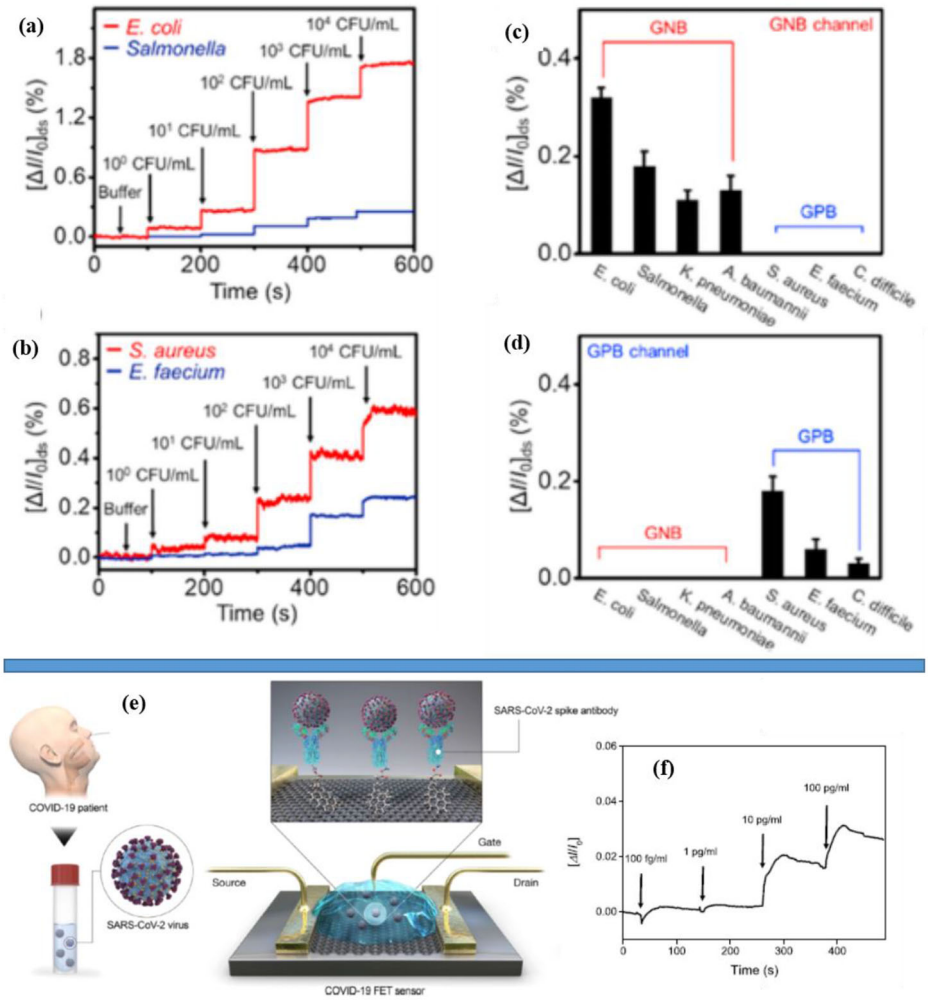

FIGURE 6 (a–d) G-FET biosensor detection of Gram-positive and Gram-negative bacteria: step-like increases in the drain-source current percentage change upon addition of (a) *E. coli* and *Salmonella* or (b) *S. aureus* and *E. faecium* at increasing concentrations from 10^0 CFU/ml to 10^4 CFU/ml and (c,d) selectivity tests for the GNB and GPB channel in the presence of both GNB and GPB bacteria resulting in a relevant signal change only in the presence of the targeted type of strain (reproduced from Ref.[49] with permission; Copyright Elsevier B.V., 2020). (e) Scheme of the G-FET biosensor reported by Seo et al. for (f) the detection of SARS-CoV-2 in human nasopharyngeal swab specimens, which appears as step-like increases in the drain-source current percentage change at increasing concentrations from 100 fg/ml to 100 pg/ml (reproduced from Ref.[10] with permission; Copyright American Chemical Society, 2020)

with the odorant-binding protein14 (OBP14) from the honey bee (*Apis mellifera*) allowed the recognition of a broad spectrum of odorants known to be attractants for bees.[62]

The field of applications is not limited to biomolecular detection. The ultrasensitive detection of disease-related exosomes can create new opportunities for clinical diagnostics since these nanovesicles can be employed as liquid biopsy biomarkers because of their high homology with their parental origin providing relevant information on multivariate diseases like cancer.[63,68] With specific antibody CD63 as a probe, Yu and coworkers achieved a 33 particles/μl LOD and employed their rGO-FET biosensor to determine exosomes in clinical serum samples discriminating among healthy and prostate cancer patients.[63] Hepatocellular carcinoma-derived microvesicles were instead detected by Wu et al.[64]

Environmental monitoring is an urgent need for modern societies,[69] where graphene-based FET biosensors can also have impact. For example, they were employed for mercury detection in mussels[42] and for revealing water pollutants (e.g., 17β-estradiol)[47] or bacteria, such as *Escherichia coli*.[48,56] A portable biosensor for detecting Gram-positive and Gram-negative bacteria (GPB and GNB) was reported by Kim et al., who used antibiotics as biorecognition probes. This platform can facilitate onsite detection and a consequent reduction of antibiotics use and the risk of emergence of antibiotics resistance.[49] As shown in Figure 6a,b, the signal associated with the percentage changes in the drain-source current exhibits clear

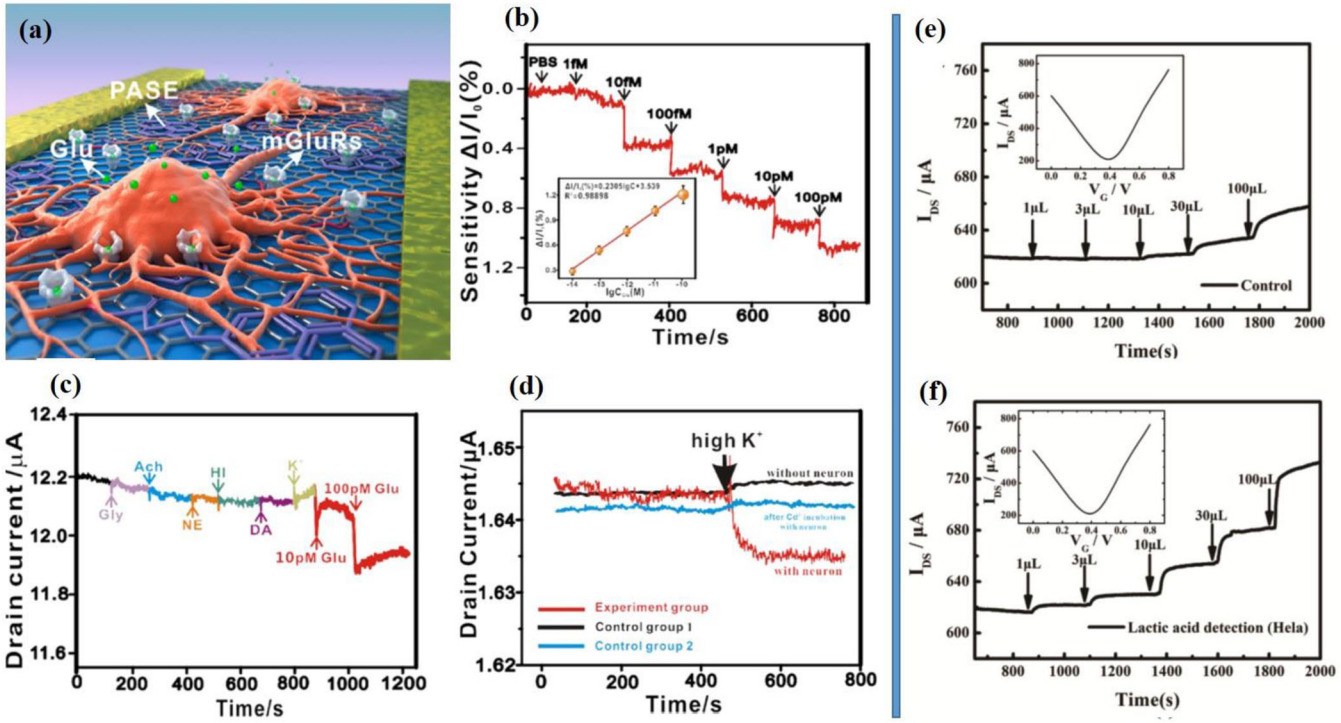

FIGURE 7 (a) Schematic of a graphene FET-based biosensor for real-time monitoring of glutamate release from primary hippocampal neurons. (b) Real-time drain current measurements at different concentrations (1, 10, and 100 fM and 1, 10, and 100 pM) of glutamate solution in cell medium. Inset: The resulting calibration curve as a function of glutamate concentrations. (c) Selectivity measurement with the addition of chemical interferents (concentration 100 pM) followed by glutamate solutions (10 and 100 pM). (d) Real-time monitoring of glutamate released from hippocampal neurons in different conditions: G-FET stimulated by high potassium stimulant (K^+) with neurons (red line), without neurons (black line), with neurons after 30 min incubation with 1 mM of calcium channel inhibitor Cd^{2+} (red line). (Reprinted with permission from Ref.[66] Copyright 2019 American Chemical Society). (e–f) Channel current response of graphene field-effect transistor for lactic acid detection in cells with a nanocomposite modified gate electrode characterized in PBS solution before and after the additions of (e) control cell medium and (f) tumor cell lines Hela of different volumes. Inset: Transfer curve of the graphene field-effect transistor measured in PBS solution (reproduced from Ref.[52] with permission; Copyright Elsevier B.V., 2020)

step-like increases (up to about 1%) when adding either GNB (*E. coli* and *Salmonella*) or GPB (*Staphylococcus aureus* and *Enterococcus faecium*) with an LOD as low as 10^0 CFU/ml. Notably, this performance is accompanied by a limited interference in the presence of nonspecific bacteria as shown in Figure 6c,d, where negligible increases are manifested in the GNB channel in the case of GPB strains (and vice versa). A dielectrophoresis-assisted detection of single antibiotic resistant bacteria was reported by Kumar et al.[50] Microfluidic components for sample handling and analyte separation can be useful tools to be integrated for increasing the impact of G-FET and rGO-FET biosensors, opening new frontiers toward precision medicine.

With the emergence of COVID-19 pandemics, considerable researchers' attention was attracted by the risk associated with the initial absence of specific drugs or vaccines. Thus, various efforts focused on developing suitable and portable tools for the rapid detection of SARS-CoV-2 in human nasopharyngeal swab specimens. In this respect, it is worth mentioning the contribution by Seo et al., who employed a G-FET biosensor for this purpose.[10] Specifically, they used SARS-CoV-2 spike antibody as molecular probe upon immobilization via a PBASE cross-linker (Figure 6e). The platform optimization proceeded in steps through detection in PBS, the acquisition of dose-dependent calibration curves, selectivity tests versus Middle East respiratory syndrome coronavirus, antigens, and then detection in universal transport medium, where nasopharyngeal swabs are routinely suspended for COVID-19 diagnosis. In terms of performance, they reported an LOD of 1.6×10^1 pfu/ml in culture medium and 2.42×10^2 copies/ml in clinical samples (Figure 6e,f).[10] The E7 protein of human papillomavirus was instead sensed in saliva by Aspermair et al.[55]

Beyond sensing, graphene-based FET biosensors can be useful tools for real-time monitoring biological processes. For instance, Zhang group demonstrated the monitoring of nitric oxide at since-cell level[65] as well as glutamate release from primary hippocampal neurons (Figure 7a–d).[66] Real-time electrical response to different

concentrations of glutamate from 1 fM to 100 pM in the cell medium is shown in Figure 7b. The authors also investigated the selectivity of their G-FET by adding interfering neurotransmitters, such as glycine (Gly), acetylcholine (Ach), norepinephrine (NE), histamine (HI), and dopamine (DA) (Figure 7c) and studied glutamate released from hippocampal neurons in different condition (Figure 7d).

Schuck et al. instead monitored the hemostasis process investigating the influence and interaction between various coagulation factors using blood samples treated with activators (vitamin K, calcium chloride, and thromboplastin reagent) and inhibitors (heparin drugs).[51] In this respect, it is worth mentioning the work by Bi et al., which reported G-FET-based lactic acid sensor transistors with a nanocomposite modified gate electrode relevant for monitoring accumulation in tumor cells through their glycolysis metabolism.[52] Indeed, these tools were applied by the authors for monitoring cell culture (Hela, A549, and HePG2) samples[52] (Figure 7e,f). The graphs reported in Figure 7e,f show relatively large channel current response to tumor cell lines Hela by adding successive volumes with respect to the control response.

5 | 2D MATERIALS-BASED FET BIOSENSORS

Graphene is characterized by a high mobility[70] and a rich physics.[71] However, its pristine form has no bandgap. Graphene bandgap engineering is possible, but on one side, it increases fabrication complexity,[72] and on the other side, it limits mobility[73] or implies the requirement for higher operating voltages.[74] For this reason (beyond a general scientific interest), other 2D materials with a proper bandgap were sought.

A valid alternative is represented by layered transition metal dichalcogenides (TMDCs),[75] with bandgap greater than 1 eV and with electronic mobility of even 200 $cm^2 V^{-1}s^{-1}$.[76] This class of 2D materials can be easily synthetized by either CVD of thin films,[77] or mechanical[78] and chemical exfoliation.[79] Among TMDCs, molybdenum disulfide (MoS_2) is so far the most widely investigated. Bulk MoS_2 is semiconducting with an indirect bandgap of 1.2 eV,[80] while single-layer MoS_2 is a direct gap semiconductor with a bandgap of 1.8 eV,[81] which is influenced (as its optical and other electronic properties) by quantum mechanical confinement in nanowires[82] and nanotubes[83] forms. In addition, layered MoS_2 does not show dangling bonds and is thermally stable up to 1400 K. Beyond physical studies on the mere monolayer MoS_2, implementation of MoS_2 sheet as channel in FETs was a recent focus of research up to dielectric-modulated FET for detection of biomolecules in a dry environment.[14c] Recent efforts are direct to stabilize the pristine device against H_2O and CO absorption and increase sensitivity by using the conjugation of a DNA tetrahedron and biotin-streptavidin. An LOD of 1 fg/ml was recently achieved for prostate-specific antigen (PSA) by Zhang et al.[84]

MoS_2 FET[9e] were reported to detect pH and streptavidin,[85] DNA,[86] IgG and PSA,[87] synthetic opioid peptides,[88] antibiotics,[89] and matrix metalloproteinase MMP-9.[90] In particular, screening of Down syndrome was achieved with MoS_2 FET biosensors by Liu et al.[91] Superior performances with respect to graphene were described.[85] In Figure 8a,b, glucose detection is illustrated in the form of step-like increases in the drain-source current upon serial additions of glucose solution, while Figure 8c shows the calibration curve at ultralow concentration indicating a 300 nM LOD.[92] Label-free early detection of miRNA as a biomarker in cancer diagnostics with detection limit of 0.03 fM was also achieved by drop-casting MoS_2 flacks suspension onto FET surface.[93]

Besides the use of mere MoS_2 sheets in transistor layouts, this TMDC was employed in combination with graphene or reduced graphene oxide[94] to fabricate an FET biosensor (Figure 8d) able to achieve 1 pM hydrogen peroxide detection as illustrated in Figure 8e. Clear steps in the percentage variation of the drain-source current are observed in the case of rGO-MoS_2 devices upon addition of increasing concentrations of H_2O_2. On the other hand, the mere rGO device exhibits a quite flat response. This striking difference is attributed to the positive charges generated after H_2O_2 addition in a process, where MoS_2 have an active role in catalyzing the decomposition of hydrogen peroxide, mimicking the reaction with horseradish peroxidase. This ability makes MoS_2 very attractive for monitoring several cellular processes involving H_2O_2, for example, as an indicator for tumor cells metabolism. Remarkably, this approach enabled the authors to evaluate in real-time H_2O_2 release from HeLa cells through MoS_2/rGO FET sensors upon stimulation with phorbol 12-myristate 13-acetate (PMA), which is able to trigger protein kinase C pathways for H_2O_2 production. Indeed, in Figure 8f, this process is evident as a sudden decrease in the red curve in the presence of HeLa cells. This change is not observed in the absence of HeLa cells (blue curve) or in the presence of a H_2O_2 scavenger, such as catalase. In terms of infectious diseases, the proof-of-concept of a large area flexible Ebola biosensor based on exfoliated MoS_2 flake was demonstrated with a detection limit in fM-pM range.[95]

Within the metal dichalcogenide class, it is worth mentioning the reports on FET biosensors based on layered rhenium disulfide (ReS_2) for pH sensing.[96] Tungsten

doi.org/10.1002/elsa.202200006

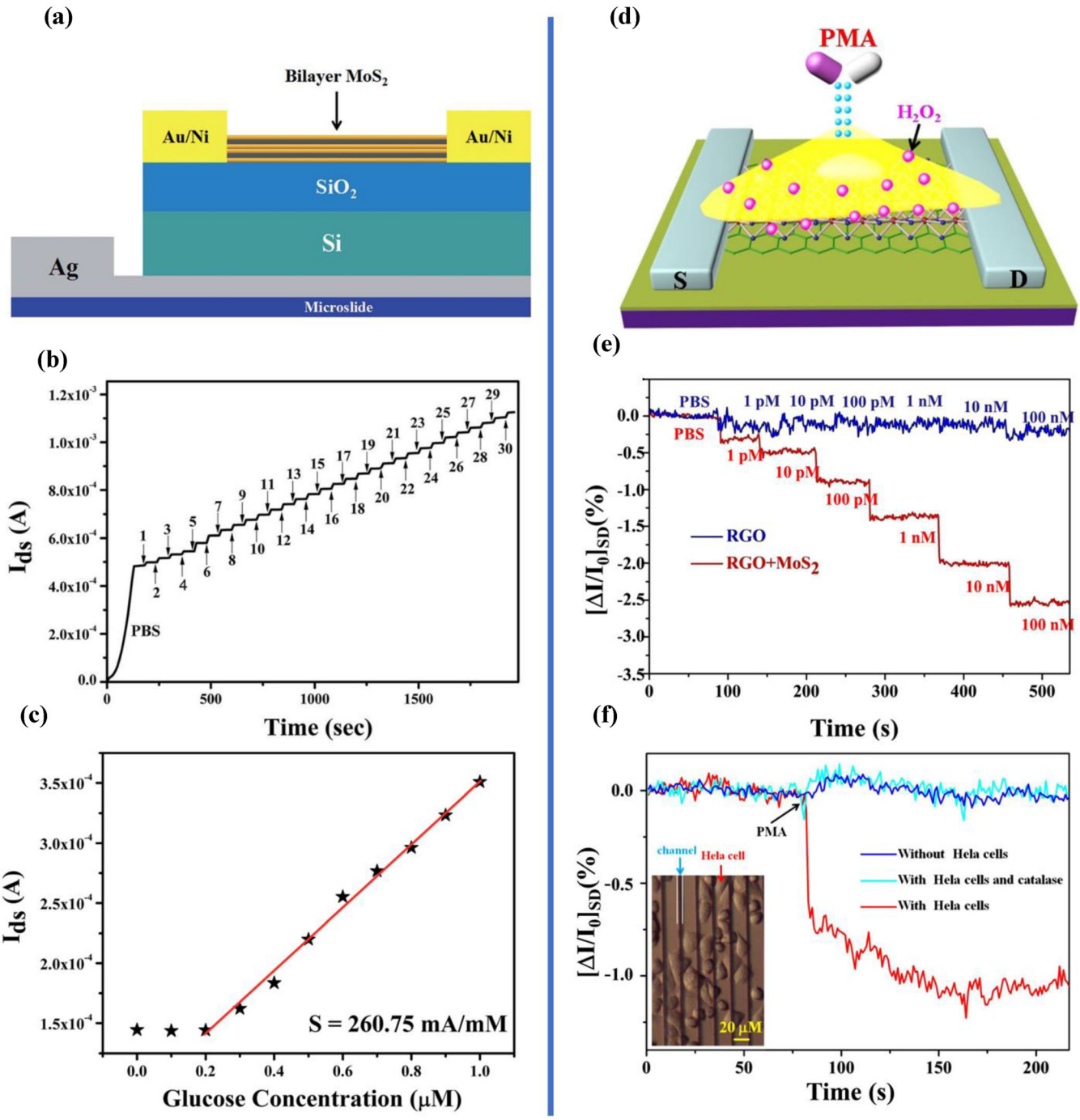

FIGURE 8 (a) Schematic diagram of a bilayer MoS_2-based FET for glucose detection. (b) Real-time current responses to changing glucose concentrations. (c) Drain current as a function of glucose concentration, which ranges from 0 to 1 mM at V_{gs} of 0.5 V and V_{ds} of 2.5 V (reproduced from Ref.[92] with permission of the Royal Society of Chemistry). (d) Schematic diagram of a MoS_2/RGO FET sensor for real-time monitoring of H_2O_2 release from cancer cell. (e) Real-time detection of H_2O_2 with increasing concentrations in PBS buffer with the MoS_2/RGO FET sensor (red line) and the mere RGO FET sensor (blue line). (f) Real-time current response of the MoS_2/RGO FET sensors toward H_2O_2 after PMA was added into PBS buffer solution in the presence of HeLa cells (red line), in the absence of HeLa cells (blue line), and when H_2O_2 scavenger catalase was mixed with the PBS solution and added onto the devices containing HeLa cells (cyan line). Inset: Optical microscope image of HeLa cells grown well on the MoS_2/RGO FET sensor array (reproduced from Ref.[94b] with permission)

doi.org/10.1002/elsa.202200006

diselenide (WSe_2) was also employed for glucose concentration evaluation[97] and for the realization of MoS_2 and WSe_2 monolayer double-gate ISFET for both pH sensing and protein detection.[98] WSe_2-based FET also represents a promising platform for the rapid and sensitive detection of SARS-CoV-2 in vitro, exhibiting a detection limit of down to 25 fg/μl in 0.01X PBS, after functionalization of the TMDC layers with monoclonal antibodies against the SARS-CoV-2 spike protein.[99] Remaining in the applications field of virus detection, 2D TMDC materials-based FETs can provide even better detection results if we consider the emerging virus detection techniques, such as isothermal amplification, rolling circle amplification, and lateral flow assays.[100] However, having the performance to avoid amplification would be an important achievement.

Another interesting member of the 2D family consists of MXenes that are exfoliated from bulk crystals composed of transition metal carbides, nitrides, or carbonitrides. The general formula is $M_{m+1}X_mT_x$, where $m = 1$, 2, or 3, M is a transition element, X is carbon or nitrogen, and T refers to surface termination group, such as OH, F, and/or O atoms. First, MXene was discovered at Drexel University in 2011,[101] and now, they have become one of the largest families of 2D materials, suitable for a variety of applications from energy storage, to polymer nanocomposite fillers, from water purification to electronic devices.[102] They exhibit high conductivity and low bandgap as graphene, although the surface area, greater than that obtainable by exfoliation of MoS_2, is less than that of graphene.[103] MXenes-based FETs have been employed for various biosensor applications. For example, a MXene platform with high sensitivity and selectivity was realized through the integration of high continuous sheets of graphene and Ti_2C with high chemical sensitivity. This heterostructure has been explored to detect influenza A H1N1 and SARS-CoV-2, demonstrating a detection limit of 150 copies/ml for H1N1 and 1 fg/ml for SARS-CoV-2 spike protein.[104] In Figure 9a, a schematic diagram of a Ti_3C_2Tx MXene-based FET for alkali detection is instead reported.[105] The Ti_3C_2Tx FET devices exhibit high selectivity to alkali even when exposed to multiple high concentration (1 M) of alkaline sodium salt (Figure 9b–d). The selectivity under high salinity condition indicates great ability in real-time and on-site alkali detection in relatively harsh environments like seawater with high ionic strength. As a further example, in Figure 9e, a schematic of the working principle of a MXene–FET device for probing action potential is shown[106]: the released neurotransmitters, as a result of action potentials firing, bind to MXene surface producing the variation of electrical signals. Conductance changes in the FET response were observed when dopamine molecules interact with the MXene surface, enabling the detection of dopamine concentration down to 0.1 μM (Figure 9f). Spiking activity was also monitored in real-time in cultured primary hippocampal neurons stimulated by a medium with high K^+ concentration and compared to recordings achieved with simultaneously-conducted calcium imaging (Figure 9g,h). The spike trains derived from electrical and optical recording exhibit a very high correlation coefficient of 0.82, validating the platform. Sweat analysis on the basis of glucose or lactate content was another area where MXenes-based FET biosensors demonstrated applicability.[107]

Finally, phosphorene (α—P, two-dimensional crystal of black phosphorus) has garnered research attention due to its direct bandgap of 1 eV (from 1.51 eV for a monolayer to 0.59 eV for five layers), reasonably high hole-dominated mobility up to 10^4 cm^2 $V^{-1}s^{-1}$, and high transport anisotropy.[108] Actually, black phosphorous (BP) nanosheets find wide application in the biomedical field since their excellent biocompatibility for use in photothermal therapy, photodynamic therapy, drug delivery, 3D printing, bioimaging, biosensing, and theranostics.[109] Moreover, embodiment of phosphorene flakes in FET layout demonstrated enhanced electron and hole transport, with high gain and noise margin, paving the way to complementary logic inverters based on ambipolar phosphorene FETs.[110] Despite the semiconductor is poorly stable in air because of oxidation, thereby hindering performance,[111] efforts are made to solve this problem, that is, through encapsulation in FET layout.[112] In this direction, a mechanically exfoliated BP biosensor was reported with passivation by a very thin film of alumina and ability to detect human immunoglobulin G (IgG) through anti-human IgG-conjugated gold nanoparticles.[113] This BP sheets biosensor demonstrated a LOD of 10 ng·ml^{-1} and fast response time on the order of seconds.

Table 3 reports an overview of the key parameters of 2D material-based FET biosensors, including some representative figures of merit. Among them, the LOD and the sensitivity and the response time are important parameters to evaluate sensor capability. Also, it has been reported if studies on specificity have been performed in the literature.

6 | SUMMARY AND OUTLOOK

In conclusion, 2D-materials FET biosensors are having a strong impact and continue to attract more and more interest. Compared to other approaches, they are characterized by specific advantages in terms of large surface-to-volume

doi.org/10.1002/elsa.202200006

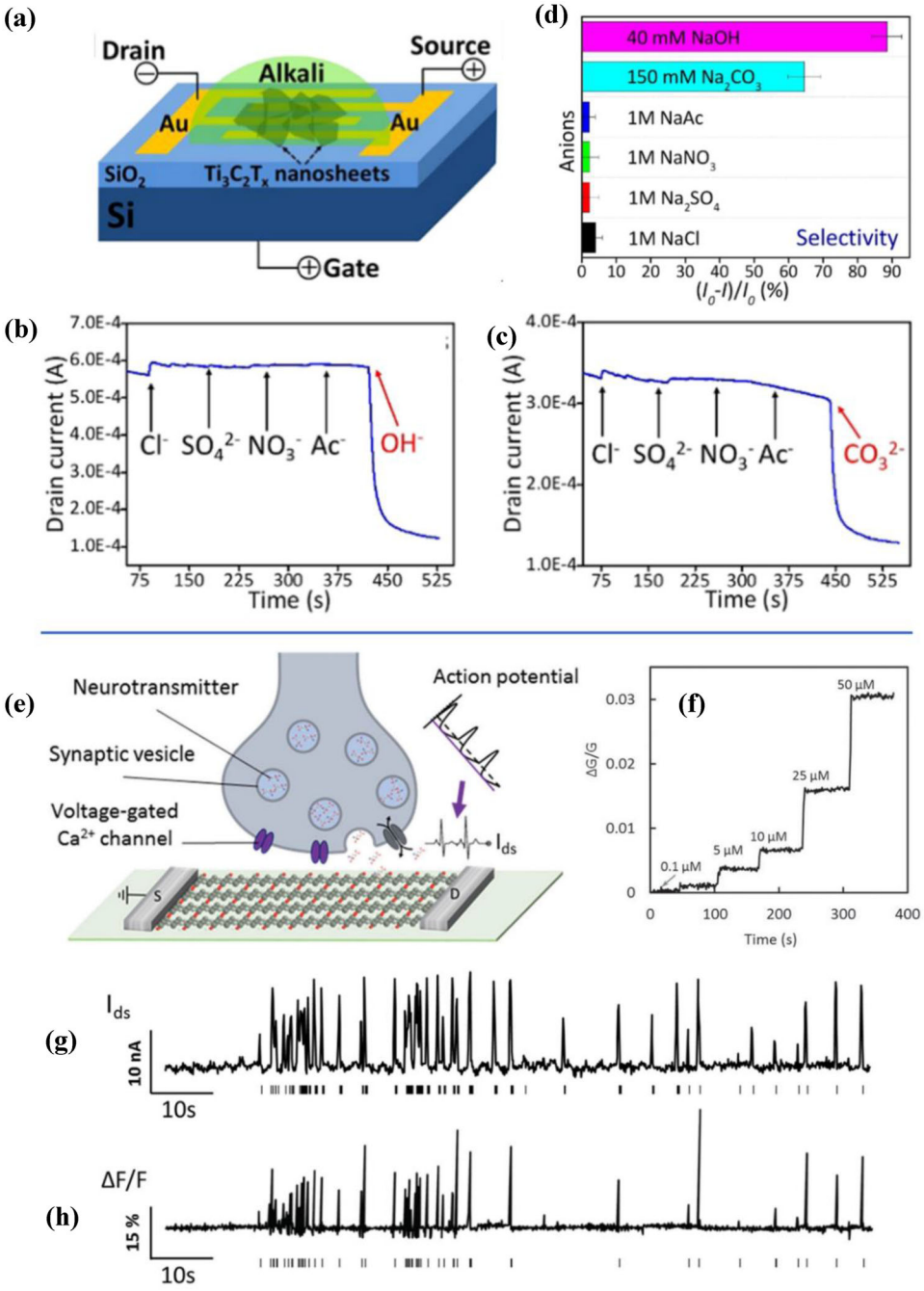

FIGURE 9 Examples for MXene-based FET biosensors. (a) Schematic diagram of a $Ti_3C_2T_x$ FET device and its (b) real-time responses under continuous addition of 40 mM NaOH and (c) 150 mM Na_2CO_3. (d) Quantification of selectivity by calculating the normalized current ($(I_0 - I)/I_0$, %) response of the device to various anions (reproduced with permission from Ref.[105] Copyright 2020 American Chemical Society). (e) Schematic of the working principle of the MXene–FET device for probing action potential and neuronal activity: neurotransmitters are released upon the firing of action potentials and bind to the MXene surface and then inducing the fluctuation of electrical signals. (f) Real-time monitoring of conductivity fluctuations of an MXene device for dopamine concentrations varying from 0.1 to 50 μM. (g) Evaluation of neuronal spiking activities by using current measurements with the MXene–FET device. (h) Simultaneously conducted recordings obtained with calcium imaging using the Fluo-4 probe to validate the functionality of the MXene-FET platform (reproduced from Ref. [106] with permission)

TABLE 3 Overview of the performances and key parameters of 2D material-based FET biosensors

2D material	Target molecule/probe	Limit of detection	Sensitivity, response, and/or related measurements	Ref.
MoS_2	pH detection streptavidin/biotin	–	$S = \Delta I/I_1 \times 100 = 713$ for a pH change between 3 and 4 (subthreshold region) $S = \Delta I/I_0 = 196$ in the subthreshold region for a streptavidin solution of 100 fM	[85]**, Δ
MoS_2	DNA target/DNA probe	10 fM	17 mV/dec in the shift of the threshold voltage V_{th}	[86]**, Δ
MoS_2	Prostate-specific antigen (PSA)/anti-PSA antibody	1 pg/ml	I_{OFF} versus PSA concentration (1 pg/ml–10 ng/ml)	[87]**, Δ
MoS_2	DAMGO synthetic opioid peptide/human μ-opioid receptor (wsMOR)	~3 nM (1.5 ng/ml)	$\Delta I/I_0$ ($V_g = 0$)% versus [DAla2, N-MePhe4, Gly-ol]-enkephalin concentration (Langmuir–Hill isotherm fit) (1 nM–100 μM)	[88]**, Δ
MoS_2	Kanamycin/aptamer DNA (APT)-complementary strand DNA (CS)	1.06 (20 s) 0.66 nM (300 s)	1.85 M^{-1} (20 s) 4.43 M^{-1} (300 s)	[89]*
MoS_2	Matrix metalloproteinase-9 (MMP-9)/amyloid-β_{1-42} ($A\beta_{1-42}$) protein probe	pM (with a ΔVth value of 0.138 V)	Linear ΔV_{th} versus MMP-9 conc. (1 pM–10 nM)	[90a]**, Δ
MoS_2	DNA target/DNA probe	0.1 fM	$\Delta R/R_0$ % versus DNA concentration 15% (at 100 aM) and 240% (at 10 fM)	[91],
MoS_2	Glucose/glucose oxidase	300 nM	260.75 mA mM^{-1}	[92]*, Δ
MoS_2/graphene	DNA target/DNA probe	10 aM	$\Delta I_{ds}(\mu A) = -2.95\ lgC_{DNA}$ (aM) −4.63 (10 aM–100 fM)	[94a],
MoS_2/RGO	H_2O_2 solution	1 pM	$\lvert\Delta I\rvert / I_0 = 0.46 lgC_{H2O2} + 5.66$ (1 pM–10 μM)	[94b],
WSe_2	Glucose/glucose oxidase (GOx)	–	$(I_{sensing} - I_{base})/I_{base}$ versus $C_{glucose}$ (1–10 mM) Max values: 6.99×10^2 A/A for 1 mM, 5.76×10^4 A/A for 5 mM, and 2.87×10^5 A/A for 10 mM	[97]Δ
ReS_2	PBS solution with different pH values	0.0132 pH	126 pH^{-1} subthreshold, 34.8 pH^{-1} saturation, 14.5 pH^{-1} linear	[96]*, Δ
$Ti_3C_2T_x$ MXene	NaOH solution also in high salinity (NaCl 2 M) environment	–	1.74 mM^{-1} (5 s) 2.01 mM^{-1} (10 s) 2.04 mM^{-1} (15 s)	[105]*
$Ti_3C_2T_x$ MXene	Dopamine	100 nM	ΔG/G versus dopamine concentration Linear modulation conductivity from 100 nM to 50 μM	[106]**, Δ
$Ti_3C_2T_x$ MXene/Prussian blue composite	Lactate and glucose	0.67×10^{-6} M (lactate sensor) 0.33×10^{-6} M (glucose sensor)	11.4 $\mu A\ mM^{-1}\ cm^{-2}$ (lactate) 35.3 $\mu A\ mM^{-1}\ cm^{-2}$ (glucose)	[107]*

Note: Typically 2D materials are single layer: for materials with double layers, the Ref. is indicated as []*, while in case of more than two layers (multilayer), the Ref. is indicated as []**. The carrier mobility, where reported, spans from 1.2 $cm^2\ (Vs)^{-1}$ (Ref.[88]) to 33.5 $cm^2\ (Vs)^{-1}$ (Ref.[92]). The I_{on}/I_{off} ratio, where reported, ranges from 3.6 (Ref.[89]) to 107 (Ref.[96]). Response time, where reported, shows a range between < 1 s (Ref.[92, 94b]) and 400 s (Ref.[91]). Selectivity experiments have been performed in all works, except those whose Ref. is indicated as $[]^{\Delta}$.

ratio, high carrier mobility, more effective local gating, high transconductance, high sensitivity, and operation at low voltages. A further advantage is the possibility to produce flexible devices.[42,114]

G-FET and rGO-FET biosensors demonstrated their potentiality for genomic sensing (with sub-fM [in some cases aM] LOD for DNA target and even short oligomers, pM for SNP), immunosensors and detection of protein biomarkers, drugs, activators, inhibitors, hormones, viruses (with fM LOD and in some cases even below), and exosomes (with responses still to be further characterized). These performances provide new opportunities for disease diagnostics, including a control of infection spreading (e.g., in the case of COVID-19 pandemics) by portable highly sensitive tools. Recent efforts are dedicated to implement fully integrated portable platforms, such as that reported by Hao et al. for on-line detection of cytokine biomarkers in saliva.[115] Such sensors can be integrated with microfluidic modules targeting a full automation of the assay reducing human intervention.

Furthermore, recent advances open new avenues for monitoring cell processes (such as H_2O_2 and various metabolites from cancer cells, glutamate release in neuronal activities, etc.), which can allow to better understand the pathophysiological aspects of various diseases and even favor the development of new drugs, included personalized therapies within the novel frontier of precision medicine. In this scenario, the new frontier can be the integration with microfluidics for high throughput and lab on chip or within microphysiological systems for screening purposes. Applications of other 2D materials are less established but already show high promises (e.g., TMDC, such as MoS_2, which combines high mobility with the ability to catalyze the decomposition of hydrogen peroxide).

The main issues toward industrialization and clinical use concern standardization, improvements in long-term stability, and reliability outside laboratory settings. In general, as in the case of other transducers, differential sensing architectures can improve the assay performances by minimizing the effect of environmental conditions or device-to-device variability.[47] Specific efforts to reduce device performance inhomogeneity were carried out by Wang et al. by fully encapsulating the graphene in a high-k dielectric layer in order to maintain the high mobility by means of an isolation of the graphene layer from contaminants in the solutions.[116] It can be expected that these aspects will require strong consideration in the next years to fully benefit of the advantages of these new, 2D-enabled technologies.

CONFLICT OF INTEREST

The authors declare no Conflicts of Interest.

ORCID

Giuseppe Maruccio https://orcid.org/0000-0001-7669-0253

REFERENCES

1. P. Bergveld, *IEEE Trans. Biomed. Eng.* **1970**, *BME-17*, 70–71.
2. P. Bergveld, *Sens. Actuators, B* **2003**, *88*, 1–20.
3. S. Caras, J. Janata, *Anal. Chem.* **1980**, *52*, 1935–1937.
4. S. V. Dzyadevych, A. P. Soldatkin, A. V. El'skaya, C. Martelet, N. Jaffrezic-Renault, *Anal. Chim. Acta* **2006**, *568*, 248–258.
5. (a) J. Janata, S. D. Moss, *Biomed. Eng.* **1976**, *11*, 241–245; (b) R. B. M. Schasfoort, R. P. H. Kooyman, P. Bergveld, J. Greve, *Biosens. Bioelectron.* **1990**, *5*, 103–124; (c) P. Fromherz, A. Offenhäusser, T. Vetter, J. Weis, *Science* **1991**, *252*, 1290–1293; (d) B. Wolf, M. Brischwein, W. Baumann, R. Ehret, M. Kraus, *Biosens. Bioelectron.* **1998**, *13*, 501–509; (e) M. Zayats, A. B. Kharitonov, E. Katz, A. F. Bückmann, I. Willner, *Biosens. Bioelectron.* **2000**, *15*, 671–680; (f) M. Zayats, O. A. Raitman, V. I. Chegel, A. B. Kharitonov, I. Willner, *Anal. Chem.* **2002**, *74*, 4763–4773.
6. (a) M. S. Makowski, A. Ivanisevic, *Small* **2011**, *7*, 1863–1875; (b) M. Kaisti, *Biosens. Bioelectron.* **2017**, *98*, 437–448; (c) Y. C. Syu, W. E. Hsu, C. T. Lin, *ECS J. Solid State Sci. Technol.* **2018**, *7*, Q3196–Q3207; (d) C. A. Vu, W. Y. Chen, *Sensors* **2019**, *19*, 4214.
7. (a) A. Nehra, K. P. Singh, *Biosens. Bioelectron.* **2015**, *74*, 731–743; (b) Y. Cui, Q. Wei, H. Park, C. M. Lieber, *Science* **2001**, *293* (5533), 1289–1292; (c) J. I. Hahm, C. M. Lieber, *Nano Lett.* **2004**, *4*, 51–54; (d) W. U. Wang, C. Chen, K.-h. Lin, Y. Fang, C. M. Lieber, *Proc. Natl. Acad. Sci. USA* **2005**, *102*, 3208; (e) H. R. Byon, H. C. Choi, *J. Am. Chem. Soc.* **2006**, *128*, 2188–2189.
8. (a) J. Rivnay, S. Inal, A. Salleo, R. M. Owens, M. Berggren, G. G. Malliaras, *Nat. Rev. Mater.* **2018**, *3*, 17086; (b) D. T. Simon, E. O. Gabrielsson, K. Tybrandt, M. Berggren, *Chem. Rev.* **2016**, *116*, 13009–13041; (c) S. Casalini, A. C. Dumitru, F. Leonardi, C. A. Bortolotti, E. T. Herruzo, A. Campana, R. F. de Oliveira, T. Cramer, R. Garcia, F. Biscarini, *ACS Nano* **2015**, *9*, 5051–5062; (d) R. A. Picca, K. Manoli, E. Macchia, L. Sarcina, C. Di Franco, N. Cioffi, D. Blasi, R. sterbacka, F. Torricelli, G. Scamarcio, L. Torsi, *Adv. Funct. Mater.* **2020**, *30*(20), 1904513; (e) J. Le Gall, F. Mouillard, T. N. Le, T. T. Vu, G. Mattana, R. Brayner, S. Zrig, V. Noel, B. Piro, *Biosens. Bioelectron.* **2020**, *157*, 112166; (f) X. Guo, Q. Q. Cao, Y. W. Liu, T. He, J. W. Liu, S. Huang, H. Tang, M. Ma, *Anal. Chem.* **2020**, *92*, 908–915; (g) N. X. Wang, A. N. Yang, Y. Fu, Y. Z. Li, F. Yan, *Acc. Chem. Res.* **2019**, *52*, 277–287.
9. (a) N. S. Green, M. L. Norton, *Anal. Chim. Acta* **2015**, *853*, 127–142; (b) T. T. Tran, A. Mulchandani, *TrAC, Trends Anal. Chem.* **2016**, *79*, 222–232; (c) S. Liu, X. F. Guo, *NPG Asia Mater.* **2012**, *4*, e23-e23; (d) S. Taniselass, M. K. M. Arshad, S. C. B. Gopinath, *Biosens. Bioelectron.* **2019**, *130*, 276–292; (e) X. R. Gan, H. M. Zhao, X. Quan, *Biosens. Bioelectron.* **2017**, *89*, 56–71; (f) H. W. Hu, A. Zavabeti, H. Y. Quan, W. Q. Zhu, H. Y. Wei, D. C. Chen, J. Z. Ou, *Biosens. Bioelectron.* **2019**, *142*, 111573.
10. G. Seo, G. Lee, M. J. Kim, S. H. Baek, M. Choi, K. B. Ku, C. S. Lee, S. Jun, D. Park, H. G. Kim, S. J. Kim, J. O. Lee, B. T. Kim, E. C. Park, S. I. Kim, *ACS Nano* **2020**, *14*, 5135–5142.
11. E. D. F. Martins, L. F. Pinotti, C. D. C. Silva, A. R. Rocha, *Chemosensors* **2021**, *9*, 30.
12. (a) E. Katz, I. Willner, *Electroanalysis* **2003**, *15*, 913–947; (b) M. S. Chiriacò, E. Primiceri, A. G. Monteduro, A. Bove, S. Leporatti, M. Capello, S. Ferri-Borgogno, R. Rinaldi, F. Novelli,

G. Maruccio, *Lab Chip* **2013**, *13*, 730–734; (c) H. H. Nguyen, J. Park, S. Kang, M. Kim, *Sensors* **2015**, *15*, 10481–10510; (d) A. J. Haes, W. P. Hall, L. Chang, W. L. Klein, R. P. Van Duyne, *Nano Lett.* **2004**, *4*, 1029–1034; (e) M. S. Chiriacò, S. Rizzato, E. Primiceri, S. Spagnolo, A. G. Monteduro, F. Ferrara, G. Maruccio, *Microelectron. Eng.* **2018**, *202*, 31–36; (f) S. Rizzato, M. Scigliuzzo, M. S. Chiriacò, P. Scarlino, A. G. Monteduro, C. Maruccio, V. Tasco, G. Maruccio, *J. Micromech. Microeng.* **2017**, *27*, 125002; (g) S. Rizzato, E. Primiceri, A. G. Monteduro, A. Colombelli, A. Leo, M. G. Manera, R. Rella, G. Maruccio, *Beilstein J. Nanotechnol.* **2018**, *9*, 1582–1593.

13. S. Kalra, M. J. Kumar, A. Dhawan, *IEEE Electron Device Lett.* **2016**, *37*, 1485–1488.
14. (a) J. Robertson, *Rep. Prog. Phys.* **2006**, *69*, 327; (b) H. S. Im, X. J. Huang, B. Gu, Y. K. Choi, *Nat. Nanotechnol.* **2007**, *2*, 430–434; (c) E. Rahman, A. Shadman, I. Ahmed, S. U. Z. Khan, Q. D. M. Khosru, *Nanotechnology* **2018**, *29*, 10; (d) K. S. Cole, R. H. Cole, *J. Chem. Phys.* **1941**, *9*, 341–351; (e) A. G. Monteduro, Z. Ameer, M. Martino, A. P. Caricato, V. Tasco, I. C. Lekshmi, R. Rinaldi, A. Hazarika, D. Choudhury, D. D. Sarma, G. Maruccio, *J. Mater. Chem. C* **2016**, *4*, 1080–1087; (f) A. G. Monteduro, Z. Ameer, S. Rizzato, M. Martino, A. P. Caricato, V. Tasco, I. C. Lekshmi, A. Hazarika, D. Choudhury, D. D. Sarma, G. Maruccio, *J. Phys. D: Appl. Phys.* **2016**, *49*, 405303; (g) Z. Ameer, A. G. Monteduro, S. Rizzato, A. P. Caricato, M. Martino, I. C. Lekshmi, A. Hazarika, D. Choudhury, E. Mazzotta, C. Malitesta, V. Tasco, D. D. Sarma, G. Maruccio, *J. Mater. Sci.-Mater. Electron.* **2018**, *29*, 7090–7098.
15. M. Voelker, P. Fromherz, *Small* **2005**, *1*, 206–210.
16. (a) P. R. Wallace, *Phys. Rev.* **1947**, *71*, 622–634; (b) G. W. Semenoff, *Phys. Rev. Lett.* **1984**, *53*, 2449–2452.
17. A. H. Castro Neto, F. Guinea, N. M. R. Peres, K. S. Novoselov, A. K. Geim, *Rev. Mod. Phys.* **2009**, *81*, 109–162.
18. A. K. Geim, *Science* **2009**, *324*, 1530–1534.
19. A. K. Geim, K. S. Novoselov, *Nat. Mater.* **2007**, *6*, 183–191.
20. A. Bolotsky, D. Butler, C. Y. Dong, K. Gerace, N. R. Glayin, C. Muratore, J. A. Robinson, A. Ebrahimi, *ACS Nano* **2019**, *13*, 9781–9810.
21. Y. F. Wang, Y. H. Xu, M. L. Hu, H. Ling, X. Zhu, *Nanophotonics* **2020**, *9*, 1601–1620.
22. N. R. Glavin, R. Rao, V. Varshney, E. Bianco, A. Apte, A. Roy, E. Ringe, P. M. Ajayan, *Adv. Mater.* **2020**, *32*, 1904302.
23. J. Kang, W. Cao, X. Xie, D. Sarkar, W. Liu, K. Banerjee, Graphene and beyond-graphene 2D crystals for next-generation green electronics, in Thomas George, M. Saiful Islam, Achyut K. Dutta (Eds.), *Micro- and Nanotechnology Sensors, Systems, and Applications VI*, International Society for Optics and Photonics, **2014**, p. 908305.
24. R. Campos, J. Borme, J. R. Guerreiro, G. Machado, M. F. Cerqueira, D. Y. Petrovykh, P. Alpuim, *ACS Sens.* **2019**, *4*, 286–293.
25. (a) S. R. Guo, J. Lin, M. Penchev, E. Yengel, M. Ghazinejad, C. S. Ozkan, M. Ozkan, *J. Nanosci. Nanotechnol.* **2011**, *11*, 5258–5263; (b) T. Y. Chen, P. T. Loan, C. L. Hsu, Y. H. Lee, J. Tse-Wei Wang, K. H. Wei, C. T. Lin, L. J. Li, *Biosens. Bioelectron.* **2013**, *41*, 103–109.
26. G. Xu, J. Abbott, L. Qin, K. Y. Yeung, Y. Song, H. Yoon, J. Kong, D. Ham, *Nat. Commun.* **2014**, *5*, 4866.
27. C. Zheng, L. Huang, H. Zhang, Z. Y. Sun, Z. Zhang, G. J. Zhang, *ACS Appl. Mater. Interfaces* **2015**, *7*, 16953–16959.
28. B. J. Cai, S. T. Wang, L. Huang, Y. Ning, Z. Y. Zhang, G. J. Zhang, *ACS Nano* **2014**, *8*, 2632–2638.
29. J. Ping, R. Vishnubhotla, A. Vrudhula, A. T. C. Johnson, *ACS Nano* **2016**, *10*, 8700–8704.
30. Z. L. Gao, H. Xia, J. Zauberman, M. Tomaiuolo, J. L. Ping, Q. C. Zhang, P. Ducos, H. C. Ye, S. Wang, X. P. Yang, F. Lubna, Z. T. Luo, L. Ren, A. T. C. Johnson, *Nano Lett.* **2018**, *18*(6), 3509–3515.
31. M. T. Hwang, Z. J. Wang, J. L. Ping, D. K. Ban, Z. C. Shiah, L. Antonschmidt, J. Lee, Y. S. Liu, A. G. Karkisaval, A. T. C. Johnson, C. H. Fan, G. Glinsky, R. Lal, *Adv. Mater.* **2018**, *30*, 1802440.
32. S. Y. Wang, M. Z. Hossain, K. Shinozuka, N. Shimizu, S. Kitada, T. Suzuki, R. Ichige, A. Kuwana, H. Kobayashi, *Biosens. Bioelectron.* **2020**, *165*, 112363.
33. Z. Hao, Y. L. Pan, C. Huang, Z. R. Wang, Q. Lin, X. Z. Zhao, S. Q. Liu, *ACS Sens.* **2020**, *5*, 2503–2513.
34. Z. Hao, Y. B. Zhu, X. J. Wang, P. G. Rotti, C. DiMarco, S. R. Tyler, X. Z. Zhao, J. F. Engelhardt, J. Hone, Q. Lin, *ACS Appl. Mater. Interfaces* **2017**, *9*, 27504–27511.
35. D. J. Kim, I. Y. Sohn, J. H. Jung, O. J. Yoon, N. E. Lee, J. S. Park, *Biosens. Bioelectron.* **2013**, *41*, 621–626.
36. Y. Kanai, Y. Ohmuro-Matsuyama, M. Tanioku, S. Ushiba, T. Ono, K. Inoue, T. Kitaguchi, M. Kimura, H. Ueda, K. Matsumoto, *ACS Sens.* **2020**, *5*, 24–28.
37. R. S. Selvarajan, R. A. Rahim, B. Y. Majlis, S. C. B. Gopinath, A. A. Hamzah, *Sensors* **2020**, *20*, 2642.
38. S. H. Liu, Y. Fu, C. Xiong, Z. K. Liu, L. Zheng, F. Yan, *ACS Appl. Mater. Interfaces* **2018**, *10*, 23522–23528.
39. S. Farid, X. Meshik, M. Choi, S. Mukherjee, Y. Lan, D. Parikh, S. Poduri, U. Baterdene, C. E. Huang, Y. Y. Wang, P. Burke, M. Dutta, M. A. Stroscio, *Biosens. Bioelectron.* **2015**, *71*, 294–299.
40. S. C. Xu, T. J. Wang, G. F. Liu, Z. X. Cao, L. A. Frank, S. Z. Jiang, C. Zhang, Z. H. Li, V. V. Krasitskaya, Q. Li, Y. J. Sha, X. M. Zhang, H. L. Liu, J. H. Wang, *Sens. Actuator, B* **2021**, *326*, 128991.
41. S. Islam, S. Shukla, V. K. Bajpai, Y. K. Han, Y. S. Huh, A. Kumar, A. Ghosh, S. Gandhi, *Biosens. Bioelectron.* **2019**, *126*, 792–799.
42. J. H. An, S. J. Park, O. S. Kwon, J. Bae, J. Jang, *ACS Nano* **2013**, *7*, 10563–10571.
43. X. Q. You, J. J. Pak, *Sens. Actuator, B* **2014**, *202*, 1357–1365.
44. E. Danielson, V. A. Sontakke, A. J. Porkovich, Z. W. Wang, P. Kumar, Z. Ziadi, Y. Yokobayashi, M. Sowwan, *Sens. Actuator, B* **2020**, *320*, 128432.
45. E. Danielson, M. Dindo, A. J. Porkovich, P. Kumar, Z. W. Wang, P. Jain, T. Mete, Z. Ziadi, R. Kikkeri, P. Laurino, M. Sowwan, *Biosens. Bioelectron.* **2020**, *165*, 112419.
46. D. H. Shin, W. Kim, J. Jun, J. S. Lee, J. H. Kim, J. Jang, *Sens. Actuator, B* **2018**, *264*, 216–223.
47. Y. J. Li, Y. B. Zhu, C. Wang, M. He, Q. Lin, *Biosens. Bioelectron.* **2019**, *126*, 59–67.
48. G. F. Wu, Z. W. Dai, X. Tang, Z. H. Lin, P. K. Lo, M. Meyyappan, K. W. C. Lai, *Adv. Healthcare Mater.* **2017**, *6*, 1700736.
49. K. H. Kim, S. J. Park, C. S. Park, S. E. Seo, J. Lee, J. Kim, S. H. Lee, S. Lee, J. S. Kim, C. M. Ryu, D. Yong, H. Yoon, H. S. Song, S. H. Lee, O. S. Kwon, *Biosens. Bioelectron.* **2020**, *167*, 112514.
50. N. Kumar, W. J. Wang, J. C. Ortiz-Marquez, M. Catalano, M. Gray, N. Biglari, K. Hikari, X. Ling, J. M. Gao, T. van Opijnen, K. S. Burch, *Biosens. Bioelectron.* **2020**, *156*, 112123.
51. A. Schuck, H. E. Kim, K. M. Jung, W. Hasenkamp, Y. S. Kim, *Biosens. Bioelectron.* **2020**, *157*, 112167.

52. Y. L. Bi, L. H. Ye, Y. Mao, L. Wang, H. Qu, J. Liu, L. Zheng, *Biosens. Bioelectron.* **2019**, *140*, 111–119.
53. S. C. Xu, C. Zhang, S. Z. Jiang, G. D. Hu, X. Y. Li, Y. Zou, H. P. Liu, J. Li, Z. H. Li, X. X. Wang, M. Z. Li, J. H. Wang, *Sens. Actuator, B* **2019**, *284*, 125–133.
54. G. E. Fenoy, W. A. Marmisolle, O. Azzaroni, W. Knoll, *Biosens. Bioelectron.* **2020**, *148*, 111796.
55. P. Aspermair, V. Mishyn, J. Bintinger, H. Happy, K. Bagga, P. Subramanian, W. Knoll, R. Boukherroub, S. Szunerits, *Anal. Bioanal. Chem.* **2021**, *413*, 779–787.
56. B. Thakur, G. H. Zhou, J. B. Chang, H. H. Pu, B. Jin, X. Y. Sui, X. C. Yuan, C. H. Yang, M. Magruder, J. H. Chen, *Biosens. Bioelectron.* **2018**, *110*, 16–22.
57. T. Beminger, C. Bliem, E. Piccinini, O. Azzaroni, W. Knoll, *Biosens. Bioelectron.* **2018**, *115*, 104–110.
58. D. Park, J. H. Kim, H. J. Kim, D. Lee, D. S. Lee, D. S. Yoon, K. S. Hwang, *Biosens. Bioelectron.* **2020**, *167*, 112505.
59. E. Piecinini, C. Bliem, C. Reiner-Rozman, F. Battaglini, O. Azzaroni, W. Knoll, *Biosens. Bioelectron.* **2017**, *92*, 661–667.
60. M. S. Chae, Y. K. Yoo, J. Kim, T. G. Kim, K. S. Hwang, *Sens. Actuator, B* **2018**, *272*, 448–458.
61. B. J. Cai, L. Huang, H. Zhang, Z. Y. Sun, Z. Y. Zhang, G. J. Zhang, *Biosens. Bioelectron.* **2015**, *74*, 329–334.
62. M. Larisika, C. Kotlowski, C. Steininger, R. Mastrogiacomo, P. Pelosi, S. Schutz, S. F. Peteu, C. Kleber, C. Reiner-Rozman, C. Nowak, W. Knoll, *Angew. Chem., Int. Ed.* **2015**, *54*, 13245–13248.
63. Y. Yu, Y. T. Li, D. Jin, F. Yang, D. Wu, M. M. Xiao, H. Zhang, Z. Y. Zhang, G. J. Zhang, *Anal. Chem.* **2019**, *91*, 10679–10686.
64. D. Wu, Y. Yu, D. Jin, M.-M. Xiao, Z.-Y. Zhang, G.-J. Zhang, *Anal. Chem.* **2020**, *92*, 4006–4015.
65. H. Xie, Y. T. Li, Y. M. Lei, Y. L. Liu, M. M. Xiao, C. Gao, D. W. Pang, W. H. Huang, Z. Y. Zhang, G. J. Zhang, *Anal. Chem.* **2016**, *88*, 11115–11122.
66. Y. T. Li, X. Jin, L. N. Tang, W. L. Lv, M. M. Xiao, Z. Y. Zhang, C. Gao, G. J. Zhang, *Anal. Chem.* **2019**, *91*, 8229–8236.
67. J. W. Park, C. Lee, J. Jang, *Sens. Actuator, B* **2015**, *208*, 532–537.
68. D. K. H. Tsang, T. J. Lieberthal, C. Watts, I. E. Dunlop, S. Ramadan, A. E. D. Hernandez, N. Klein, *Sci. Rep.* **2019**, *9*, 13946.
69. S. Rizzato, A. Leo, A. G. Monteduro, M. S. Chiriacò, E. Primiceri, F. Sirsi, A. Milone, G. Maruccio, *Micromachines* **2020**, *11*, 491.
70. K. I. Bolotin, K. J. Sikes, Z. Jiang, M. Klima, G. Fudenberg, J. Hone, P. Kim, H. L. Stormer, *Solid State Commun.*. **2008**, *146*, 351–355.
71. K. S. Novoselov, A. K. Geim, S. V. Morozov, D. Jiang, M. I. Katsnelson, I. V. Grigorieva, S. V. Dubonos, A. A. Firsov, *Nature* **2005**, *438*, 197–200.
72. M. S. Nevius, M. Conrad, F. Wang, A. Celis, M. N. Nair, A. Taleb-Ibrahimi, A. Tejeda, E. H. Conrad, *Phys. Rev. Lett.* **2015**, *115*, 5.
73. M. Y. Han, B. Ozyilmaz, Y. B. Zhang, P. Kim, *Phys. Rev. Lett.* **2007**, *98*, 4.
74. F. N. Xia, D. B. Farmer, Y. M. Lin, P. Avouris, *Nano Lett.* **2010**, *10*, 715–718.
75. A. Rawat, N. Jena, A. Dimple De Sarkar, *J. Mater. Chem. A* **2018**, *6*, 8693–8704.
76. S. H. Mir, V. K. Yadav, J. K. Singh, *ACS Omega* **2020**, *5*, 14203–14211.
77. Y. H. Lee, X. Q. Zhang, W. J. Zhang, M. T. Chang, C. T. Lin, K. D. Chang, Y. C. Yu, J. T. W. Wang, C. S. Chang, L. J. Li, T. W. Lin, *Adv. Mater.* **2012**, *24*, 2320–2325.
78. K. S. Novoselov, D. Jiang, F. Schedin, T. J. Booth, V. V. Khotkevich, S. V. Morozov, A. K. Geim, *Proc. Natl. Acad. Sci. USA* **2005**, *102*, 10451–10453.
79. G. Eda, H. Yamaguchi, D. Voiry, T. Fujita, M. W. Chen, M. Chhowalla, *Nano Lett.* **2011**, *11*, 5111–5116.
80. K. K. Kam, B. A. Parkinson, *J. Phys. Chem.* **1982**, *86*, 463–467.
81. K. F. Mak, C. Lee, J. Hone, J. Shan, T. F. Heinz, *Phys. Rev. Lett.* **2010**, *105*, 4.
82. M. Remskar, A. Mrzel, Z. Skraba, A. Jesih, M. Ceh, J. Demsar, P. Stadelmann, F. Levy, D. Mihailovic, *Science* **2001**, *292*, 479–481.
83. Y. Feldman, E. Wasserman, D. J. Srolovitz, R. Tenne, *Science* **1995**, *267*, 222–225.
84. Y. Zhang, D. Z. Feng, Y. Xu, Z. W. Yin, W. Dou, U. E. Habiba, C. Y. Pan, Z. K. Zhang, H. Mou, H. Y. Deng, X. Q. Mi, N. Dai, *Appl. Surf. Sci.* **2021**, *548*, 7.
85. D. Sarkar, W. Liu, X. J. Xie, A. C. Anselmo, S. Mitragotri, K. Banerjee, *ACS Nano* **2014**, *8*, 3992–4003.
86. D. W. Lee, J. Lee, I. Y. Sohn, B. Y. Kim, Y. M. Son, H. Bark, J. Jung, M. Choi, T. H. Kim, C. Lee, N. E. Lee, *Nano Res.* **2015**, *8*, 2340–2350.
87. J. Lee, P. Dak, Y. Lee, H. Park, W. Choi, M. A. Alam, S. Kim, *Sci. Rep.* **2014**, *4*, 7352.
88. C. H. Naylor, N. J. Kybert, C. Schneier, J. Xi, G. Romero, J. G. Saven, R. Y. Liu, A. T. C. Johnson, *ACS Nano* **2016**, *10*, 6173–6179.
89. X. Y. Chen, S. B. Hao, B. Y. Zong, C. B. Liu, S. Mao, *Biosens. Bioelectron.* **2019**, *145*, 111711.
90. (a) H. Park, H. Lee, S. H. Jeong, E. Lee, W. Lee, N. Liu, D. S. Yoon, S. Kim, S. W. Lee, *Anal. Chem.* **2019**, *91*, 8252–8258; (b) X. Gan, H. Zhao, X. J. B. Quan, *Biosens. Bioelectron.* **2017**, *89*, 56–71.
91. J. X. Liu, X. H. Chen, Q. Q. Wang, M. M. Xiao, D. L. Zhong, W. Sun, G. Y. Zhang, Z. Y. Zhang, *Nano Lett.* **2019**, *19*, 1437–1444.
92. J. J. Shan, J. H. Li, X. Y. Chu, M. Z. Xu, F. J. Jin, X. J. Wang, L. Ma, X. Fang, Z. P. Wei, X. H. Wang, *RSC Adv.* **2018**, *8*, 7942–7948.
93. S. M. Majd, A. Salimi, F. Ghasemi, *Biosens. Bioelectron.* **2018**, *105*, 6–13.
94. (a) S. Chen, Y. Sun, Y. P. Xia, K. Lv, B. Y. Man, C. Yang, *Biosens. Bioelectron.* **2020**, *156*, 112128; (b) C. Zheng, X. Jin, Y. T. Li, J. C. Mei, Y. J. Sun, M. M. Xiao, H. Zhang, Z. Y. Zhang, G. J. Zhang, *Sci. Rep.* **2019**, *9*, 759.
95. P. Zhang, S. Yang, R. Pineda-Gómez, B. Ibarlucea, J. Ma, M. R. Lohe, T. F. Akbar, L. Baraban, G. Cuniberti, X. J. S. Feng, *Small* **2019**, *15*, 1901265.
96. W. G. Liao, W. Wei, Y. Tong, W. K. Chim, C. X. Zhu, *ACS Appl. Mater. Interfaces* **2018**, *10*, 7248–7255.
97. H. W. Lee, D. H. Kang, J. H. Cho, S. Lee, D. H. Jun, J. H. Park, *ACS Appl. Mater. Interfaces* **2018**, *10*, 17639–17645.
98. A. Shadman, E. Rahman, Q. D. J. S. Khosru, B.-S. Research, *Sens. Bio-Sens. Res.***2016**, *11*, 45–51.
99. P. Fathi-Hafshejani, N. Azam, L. Wang, M. A. Kuroda, M. C. Hamilton, S. Hasim, M. Mahjouri-Samani, *ACS Nano* **2021**, *15*, 11461–11469.
100. C. Menard-Moyon, A. Bianco, K. Kalantar-Zadeh, *ACS Sens.* **2020**, *5*, 3739–3769.

101. M. Naguib, M. Kurtoglu, V. Presser, J. Lu, J. J. Niu, M. Heon, L. Hultman, Y. Gogotsi, M. W. Barsoum, *Adv. Mater.* **2011**, *23*, 4248–4253.
102. B. Z. Xu, C. Y. Zhi, P. Shi, *J. Phys. Mater.* **2020**, *3*, 7.
103. R. Khan, S. Andreescu, *Sensors* **2020**, *20*, 5434.
104. Y. X. Li, Z. K. Peng, N. J. Holl, M. R. Hassan, J. M. Pappas, C. J. Wei, O. H. Izadi, Y. Wang, X. Y. Dong, C. Wang, Y. W. Huang, D. Kim, C. L. Wu, *ACS Omega* **2021**, *6*, 6643–6653.
105. C. B. Liu, S. B. Hao, X. Y. Chen, B. Y. Zong, S. Mao, *ACS Appl. Mater. Interfaces* **2020**, *12*, 32970–32978.
106. B. Z. Xu, M. S. Zhu, W. C. Zhang, X. Zhen, Z. X. Pei, Q. Xue, C. Y. Zhi, P. Shi, *Adv. Mater.* **2016**, *28*, 3333–3339.
107. Y. J. Lei, E. N. Zhao, Y. Z. Zhang, Q. Jiang, J. H. He, A. Baeumner, O. S. Wolfbeis, Z. L. Wang, K. N. Salama, H. N. Aishareef, *Small* **2019**, *15*, 1901190.
108. J. S. Qiao, X. H. Kong, Z. X. Hu, F. Yang, W. Ji, *Nat. Commun.* **2014**, *5*, 7.
109. M. M. Luo, T. J. Fan, Y. Zhou, H. Zhang, L. Mei, *Adv. Funct. Mater.* **2019**, *29*, 19.
110. S. Das, M. Demarteau, A. Roelofs, *ACS Nano* **2014**, *8*, 11730–11738.
111. R. Gusmao, Z. Sofer, M. Pumera, *Angew. Chem., Int. Ed.* **2017**, *56*, 8052–8072.
112. Y. Y. Illarionov, M. Waltl, G. Rzepa, T. Knobloch, J. S. Kim, D. Akinwande, T. Grasser, *npj 2D Mater. Appl.* **2017**, *1*, 7.
113. Y. T. Chen, R. Ren, H. H. Pu, J. B. Chang, S. Mao, J. H. Chen, *Biosens. Bioelectron.* **2017**, *89*, 505–510.
114. Y. H. Kwak, D. S. Choi, Y. N. Kim, H. Kim, D. H. Yoon, S. S. Ahn, J. W. Yang, W. S. Yang, S. Seo, *Biosens. Bioelectron.* **2012**, *37*, 82–87.
115. Z. Hao, Y. L. Pan, W. W. Shao, Q. Lin, X. Z. Zhao, *Biosens. Bioelectron.* **2019**, *134*, 16–23.
116. C. Wang, J. J. Wu, Y. S. He, Z. Song, S. M. Shi, Y. B. Zhu, Y. Jia, W. X. Ye, *Nano Lett.* **2020**, *20*, 166–175.

How to cite this article: S. Rizzato, A. G. Monteduro, A. Leo, M. T. Todaro, G. Maruccio, *Electrochem Sci Adv* **2022**, e2200006. https://doi.org/10.1002/elsa.202200006